Wageningen University
University of Twente

Master's thesis

Optimizing transport properties in TM5 using SF_6

Author
Emma van der Veen

Supervisor
Dr. Wouter Peters

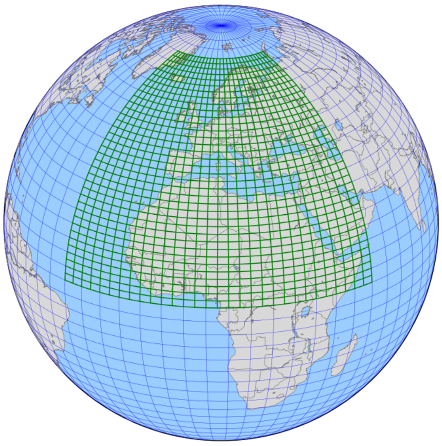

May 27, 2013

Document title	Optimizing transport properties in TM5 using SF_6 *Master's thesis for the master program Climate Studies at Wageningen University and the master program Applied Mathematics at the University of Twente*
Date	May 27, 2013
Author	Emma van der Veen emmavdv@gmail.com +31 (0)6 488 32 342
Assessment Committee	Dr. W. Peters Prof. dr. M. Krol
Wageningen University	Department Meteorology and Air Quality
Assessment Committee	Dr. A. Zagaris Prof. dr. S. A. van Gils Prof. dr. ir. B. J. Geurts
University of Twente	Department Applied Analysis and Mathematical Physics

Abstract

Increasingly, global chemistry transport models are used to estimate sources and sinks (fluxes) of CO_2 with a data-assimilation (DA) approach. A recent transport model intercomparison study shows that vertical mixing, implemented differently in the various transport models, strongly influences the estimated carbon fluxes. Therefore, improving vertical (and horizontal) transport in such models is required. In this study, we focus on horizontal transport in the global chemistry Transport Model, version 5 (TM5) with simulations of the anthropogenic compound SF_6. As many other transport models, TM5 simulates too slow interhemispheric mixing of trace gasses, and hence overestimates the observed concentration gradient between the Northern and Southern Hemispheres. To tackle the problem, we firstly examine the performance of a DA system, namely the Ensemble Kalman Filter, in estimating fluxes and transport properties in a 1-D advection-diffusion model. Hereafter, we improve transport in TM5 by tuning horizontal difusivity of the numerical scheme. Lastly, we aim to capture an actual process that represents (extra) horizontal transport, and parameterize it as a diffuse process in strong convective areas. We demonstrate an optimal value for the transport parameter by optimization with the Carbon Tracker Data Assimilation System (CTDAS). Both the numerical adjustment and the parameterization improve interhemispheric mixing in TM5, as we also validate with independent aircraft data.

Preface

The work that I present here is the result of a ten month project that I conducted for both the master's specialization Applied Analysis and Mathematical Physics (AAMP) at the University of Twente (UT) and the track Meteorology and Air Quality (MAQ) at Wageningen University (WUR).

After having studied math for four years, and climate in the next, I had to decide on a thesis subject. In Wageningen, Wouter Peters, my supervisor, introduced me to the concept of inverse modeling and global transport models for trace gasses, and I became enthusiastic to work on the topic. Wouter Peters(on behalf of the MAQ department), and Stephan van Gils and Antonios Zagaris (on behalf of the AAMP department) supported my ambition to perform this research for both masters, for which I am grateful. I conducted my work at the MAQ department, and the months flew by. In the first place since I found the research topic interesting and enjoyed the work, but moreover due to the guidance of my supervisor. I thank Wouter Peters for the pleasant meetings - which he always made the time for despite his own busy schedule -, his enthusiasm during the project, and the extensive and constructive feedback on my work. Also, involving me in the TM5 community activities, allowed me to experience science in a different way. I learned so many things (from python to atmospheric modeling to 'telling a - scientific - story') in these past ten months, thanks for that!

The working environment at the department was friendly and encouraging. I thank Ingrid van der Laan-Luijkx for helping me during my (first) experiences with the Carbon Tracker Data-Assimilation System (CTDAS), and Ivar van der Velde for preparing input data and helping me out with the system as well! And of course Maarten Krol for discussions on my work and explanations about TM5. Besides, I thank Ken Masarie from the National Oceanic and Atmospheric Administration (NOAA) for preparing and providing the SF_6 obspack data set that I used for my simulations. Also, Sourish Basu and Sander Houweling from the Space Research Organization Netherlands (SRON) were so kind to provide the code that I used as the basis of my parameterization scheme. Thanks.

As for the department in Enschede, I thank Antonios Zagaris for his useful feedback on my report and both Stephan van Gils and Antonios Zagaris for the pleasant cooperation. I highly appreciate it that you gave me the opportunity to choose my own (study) path. Also, I thank Bernhard Geurts for taking part in my assessment committee.

Lastly, I thank my boyfriend Rob, my family, and friends for their support during this project.

Contents

Abstract

Preface

Chapter 1

Introduction

The Industrial Revolution, starting halfway the 18th century, led to a cascade of technological developments in different fields, a process that continues up to the present day. Already from the 19th century, but even more evident from the mid 20th century, human activities lead to a significant increase of carbon dioxide (CO_2) concentrations in the atmosphere. Main causes are emissions released by the combustion of fossil fuels - such as coal, natural gas, and oil - for energy use and transportation purposes, but industrial processes or land use change (e.g. deforestation or the conversion of forest into agricultural land) play a role as well. These 'anthropogenic' emissions are still growing and start to affect the human environment, a concept that is known as 'climate change'. Well-known consequences are the worldwide observed trends of temperature increase and sea level rise over the past decades, but these are not the only problems. Increasing atmospheric CO_2 concentrations are tightly linked with for instance ocean acidification and the loss of marine biodiversity. Also, melting of permafrost soils - due to temperature increase - will release large amounts of CO_2, and in this way accelerate the process.

Luckily for us humans, the globe is believed to have a strong buffering capacity. About half of the anthropogenic CO_2 emissions are taken up by the terrestrial biosphere and the oceans each year. Unfortunately, the location and (future) magnitude of the uptake are still unknown and require a better understanding of the global carbon cycle. The atmospheric concentration of CO_2 is determined by sources, adding CO_2 to it (positive flux), and sinks, taking up CO_2 (negative flux). Increasingly, data-assimilation systems are used to estimate these carbon fluxes. They incorporate observations and simulated values of CO_2, and infer the fluxes via inverse modeling. Transport models are an important part of data-assimilation since they calculate the atmospheric transport of trace gasses (less common gasses in Earth's atmosphere, e.g. CO_2).

Even though data-assimilation systems are under development for many years, the outcomes concerning the size and distribution of CO_2 fluxes remain uncertain (Gurney et al., 2002). This uncertainty is particularly caused by the variety of transport models that is contained in the assimilation methods (Denning et al., 1999). For instance, different transport models use different difusivity to transport trace gasses and no consensus on the right transport settings is reached yet. That improvement of transport models in this respect is important is stated in a recent paper by Stephens et al. (2007). With an inter-comparison study they show that large variations in estimated northern and tropical land fluxes exist between different model studies.

Most importantly, they demonstrate that these variations are systematically related to the vertical gradient - of CO_2 in the Northern Hemisphere - that is used in the different transport models. The main cause is the tight link between atmospheric mixing, surface CO_2 fluxes, and spatial gradients in the inversion method of data-assimilation systems. For instance, when the magnitude of a source (emitter of the trace gas) is estimated via inverse modeling, a transport model with weak vertical mixing (such that a relatively large amount of tracer is trapped near the surface) would infer weaker emissions to match surface observations than a transport model with strong vertical mixing (and lower concentrations near the surface). Vice versa, sink regions require a stronger uptake when estimated with weak mixing in a transport model, than with strong mixing.

In this way, biases in (vertical) transport in the tracer transport models automatically result in biases in estimated fluxes of CO_2 (Stephens et al., 2007). The recommendation of Stephens et al. (2007) is therefore to further investigate, and improve, vertical and horizontal transport of trace gasses in transport models. This is what we do in this research. Specifically, we focus on the fifth version of the global chemistry Transport Model (TM5), and its horizontal transport properties. Namely, a main problem in TM5, and in most other transport models as well, is too slow interhemispheric mixing (mixing of air between the Northern and Southern Hemispheres, also 'meridional' or 'north-south' transport) of trace gasses. By optimizing horizontal transport with the CarbonTracker Data Assimilation System (CTDAS) we aim to improve this property in TM5, and contribute to better carbon dioxide flux estimates in the future.

The main objectives of this study are:

1. To assess the performance of CTDAS in optimizing specific (transport) parameters in a simplified transport model.

Chapter 2 explains the theory behind CTDAS (the Ensemble Kalman Filter). We design a simplified transport model, and describe it in Chapter 3. Chapter 4 combines the theory and transport model, and evaluates the performance of CTDAS in an experiment.

2. To determine methods to enhance horizontal transport in TM5.

From the simplified model, we switch to TM5. Chapter 5 explains its main properties, and the two relevant tracer transport routines: the advection and convection routine. In Chapter 6, we provide background information on the chemical tracer sulfur hexafluoride (SF_6), and herewith illustrate the problem of slow interhemispheric transport in TM5. Also, we explain two methods that we use to enhance horizontal transport. The first tunes horizontal numerical diffusion in the model, whereas the second aims to capture the physical process with a parameterization.

3. To optimize the transport parameter (determining the strength of horizontal transport in the parameterization scheme) with SF_6 simulations in CTDAS.

Chapter 7 explains the setup of the CTDAS optimizations. First, we optimize one global transport parameter, and aim to capture temporal variations in transport. Second, we investigate the optimization of multiple transport parameters in order to capture spatial variations. From both evaluations, we determine a suitable parameter value to parameterize horizontal diffusion in TM5.

4. To validate the results with independent observations.

Chapter 8 verifies that the transport parameter value we determine does not only improve SF_6 simulations for observations that are used in the optimization, but for independent measurements as well.

In Chapter 9 we look back at this research, discuss assumptions we made in the methods, and evaluate relevant details in the results. Also, we identify points of attention in the procedure and outcomes of the CTDAS optimizations. Chapter 10 states the conclusions. Chapter 11 lists our recommendations for further research.

Chapter 2

The CarbonTracker data-assimilation system

The method that the CarbonTracker data-assimilation system, from here on referred to as CTDAS, uses to assimilate parameters (these are specified later) is called the Ensemble Kalman Filter (EnKF). Evensen (1994a,b) presented the initial method, and additionally wrote a paper providing an overview of the implementation and use of the filter (Evensen, 2003). We use these, and papers presented by Houtekamer and Mitchell (1998), and by Peters et al. (2005), to give an introduction to the Ensemble Kalman Filter.

Section 1 presents a cost function, that describes the relation between observations, a priori, and current state vector parameters, and explains how to minimize the costs involved with a state vector update. Furthermore, Section 2 discusses the use of an ensemble to represent covariances of a priori parameters.

1 Cost function and state vector update

A state vector contains the parameters that are optimized by the Ensemble Kalman Filter. This vector is the input of the transport model, and thus determines the modeled concentrations. The purpose of the data-assimilation system is to find parameter values that minimize the error between observed and modeled concentrations, regarding the observational uncertainty. However, the parameter values should not deviate too much from the a priori known/assumed state, regarding uncertainty of the a priori values. A a cost function J, forming the basis of the filter's analysis, considers both parts:

$$J(\mathbf{x}) = (\mathbf{x} - \mathbf{x_0})^{\mathrm{T}} \cdot \mathbf{P}^{-1} \cdot (\mathbf{x} - \mathbf{x_0}) + (\mathbf{y} - \mathcal{H}(\mathbf{x}))^{\mathrm{T}} \cdot \mathbf{R}^{-1} \cdot (\mathbf{y} - \mathcal{H}(\mathbf{x}))\,. \tag{2.1}$$

Here, the cost function J is a function of a state vector $\mathbf{x}$ $[m \times 1]$. It considers the difference between the state vector $\mathbf{x}$ and its a priori known/assumed version $\mathbf{x_0}$ $[m \times 1]$, regarding covariances in the a priori parameter values in $\mathbf{P}$ $[m \times m]$. Furthermore, the second term indicates the difference between observations $\mathbf{y}$ $[n \times 1]$ and the modeled concentrations $\mathcal{H}(\mathbf{x})$ $[n \times 1]$. The diagonal of $\mathbf{R}$ $[n \times n]$ contains the variances of observations at the different measurement stations. Finally, $\mathcal{H}$ is the transport model that provides (modeled) concentrations given a certain state vector input.

Section 2 explains that the state vector $\mathbf{x_0}$ with covariance $\mathbf{P}$ are actually approximated by multiple state vectors that are distributed according to a Gaussian probability density function (PDF). Still, it is important to state in this section already, since it assures that maximizing the probability of the state vector is equivalent with minimizing the cost function J (Chatterjee and Michalak, 2013):

$$\nabla J(\mathbf{x_{opt}}) = 0. \tag{2.2}$$

The solution to (2.2) is calculated with a least squares approach such that:

$$\mathbf{P_0}^{\text{-1}} \cdot (\mathbf{x_{opt}} - \mathbf{x_0}) - \mathbf{H}^{\mathrm{T}}\mathbf{R}^{\text{-1}} \cdot (\mathbf{y} - \mathcal{H}(\mathbf{x_{opt}})) = 0. \tag{2.3}$$

Here, $\mathbf{x_{opt}}$ is the state vector that optimizes the cost function, considering its initial state $\mathbf{x_0}$. Furthermore, $\mathbf{H}$ $[m \times n]$ is the linearized matrix form of the operator (or transport model) $\mathcal{H}$. Note that $\mathbf{P}$, $\mathbf{R}$, and $\mathbf{y}$ are the same as before.

Evaluation of (2.3) provides that:

$$\mathbf{x_{opt}} = \mathbf{x_0} + \mathbf{K}\left(\mathbf{y} - \mathcal{H}(\mathbf{x_0})\right), \tag{2.4}$$

with

$$\mathbf{K} = \mathbf{P_0}\mathbf{H}^{\mathrm{T}}(\mathbf{H}\mathbf{P_0}\mathbf{H}^{\mathrm{T}} + \mathbf{R})^{\mathrm{T}}. \tag{2.5}$$

Since $\mathbf{K}$ $[m \times n]$ determines the update of the state vector, it is often referred to as the 'Kalman gain matrix'. Besides, it determines the update of the a priori covariance matrix:

$$\mathbf{P_{opt}} = (\mathbf{I} - \mathbf{K}\mathbf{H})\mathbf{P_0}. \tag{2.6}$$

We explain the derivation of this update by expressing $\mathbf{P}$ in terms of the a priori and observational errors. Therefore, we define:

$$\begin{array}{lll} \epsilon_p = \mathbf{x_0} - \mathbf{x_{real}} & \text{s.t.} & \mathbb{E}[\epsilon_p {\epsilon_p}^{\mathrm{T}}] = \mathbf{P}; \\ \epsilon_r = \mathbf{y} - \mathcal{H}(\mathbf{x_{real}}) & \text{s.t.} & \mathbb{E}[\epsilon_r {\epsilon_r}^{\mathrm{T}}] = \mathbf{R}, \end{array} \tag{2.7}$$

with ϵ_p the error between the prior and the real state, and ϵ_r the error between the observations and modeled concentrations obtained with the real state vector.

By combining (2.4) and (2.7), we find that:

$$\begin{aligned} \epsilon_{opt} &= \mathbf{x_{opt}} - \mathbf{x_{real}}, \\ &= \epsilon_p + \mathbf{K}\left(\mathbf{y} - \mathcal{H}(\mathbf{x_0})\right), \\ &= \epsilon_p + \mathbf{K}\left(\mathbf{y} - \mathcal{H}(\mathbf{x_{real}}) + \mathbf{H}(\mathbf{x_{real}} - \mathbf{x_0})\right), \\ &= (\mathbf{I} - \mathbf{K}\mathbf{H})\epsilon_p + \mathbf{K}\epsilon_r. \end{aligned} \tag{2.8}$$

Note that we linearize $\mathcal{H}$ in the second step. To obtain the updated covariance matrix, we do:

$$\begin{aligned} \mathbf{P_{opt}} &= \mathbb{E}\left[\epsilon_{opt}{\epsilon_{opt}}^{\mathrm{T}}\right], \\ &= \mathbb{E}\big[(\mathbf{I} - \mathbf{K}\mathbf{H})\epsilon_p{\epsilon_p}^{\mathrm{T}}(\mathbf{I} - \mathbf{K}\mathbf{H})^{\mathrm{T}} + \mathbf{K}\epsilon_r{\epsilon_p}^{\mathrm{T}}(\mathbf{I} - \mathbf{K}\mathbf{H})^{\mathrm{T}} \\ &\qquad\qquad + (\mathbf{I} - \mathbf{K}\mathbf{H})\epsilon_p{\epsilon_r}^{\mathrm{T}}\mathbf{K}^{\mathrm{T}} + \mathbf{K}\epsilon_r{\epsilon_r}^{\mathrm{T}}\mathbf{K}^{\mathrm{T}}\ \big], \\ &= (\mathbf{I} - \mathbf{K}\mathbf{H})\mathbf{P}(\mathbf{I} - \mathbf{K}\mathbf{H})^{\mathrm{T}} + \mathbf{K}\mathbf{R}\mathbf{K}^{\mathrm{T}}. \end{aligned} \tag{2.9}$$

The last step is allowed, since the errors in a priori states and observations are independent: $\mathbb{E}[\epsilon_p{\epsilon_r}^{\mathrm{T}}] = \mathbb{E}[\epsilon_p{\epsilon_r}^{\mathrm{T}}] = 0$.

By proving that:

$$-(\mathbf{I} - \mathbf{K}\mathbf{H})\mathbf{P}\mathbf{H}^{\mathrm{T}}\mathbf{K}^{\mathrm{T}} + \mathbf{K}\mathbf{R}\mathbf{K}^{\mathrm{T}} = 0, \tag{2.10}$$

we arrive at the covariance matrix update as in (2.6).

2 Ensemble members

When the filter from Section 1 optimizes a state vector with many (m) parameters, one can imagine that especially steps (2.5) and (2.6) become computationally expensive, if not impossible. To avoid this problem, the Ensemble Kalman Filter represents the covariance matrix $\mathbf{P}$ in fewer (N) dimensions. The ensemble created consists of N state vector members, divided in a mean (of the ensemble) and deviations from the mean:

$$\mathbf{x}_i = \bar{\mathbf{x}} + \mathbf{x}'_i, \tag{2.11}$$

for $i = 1, \ldots, N$ members.

Of (2.11), mainly the deviations are important, since they represent the spread in the ensemble. They are obtained by taking the square root of $\mathbf{P}$:

$$\mathbf{P} = \mathbf{X}\mathbf{X}^{\mathrm{T}}. \tag{2.12}$$

Here, $\mathbf{X}$ is a $[m \times N]$ matrix and the ensemble of deviations is chosen such that:

$$\begin{aligned} \mathbf{X} &= \tfrac{1}{\sqrt{N-1}}(\mathbf{x}_1 - \bar{\mathbf{x}}, \mathbf{x}_2 - \bar{\mathbf{x}}, \ldots, \mathbf{x}_N - \bar{\mathbf{x}})^{\mathrm{T}}, \\ &= \tfrac{1}{\sqrt{N-1}}(\mathbf{x}'_1, \mathbf{x}'_2, \ldots, \mathbf{x}'_N)^{\mathrm{T}}. \end{aligned} \tag{2.13}$$

The representation of $\mathbf{P}$ as in (2.12) and (2.13) is an approximation that improves with N, and becomes exact for an infinite number of ensemble members ($N \rightarrow \infty$). The ensemble members are chosen according to a normal distribution and hence define the Gaussian PDF of the state vector $\mathbf{x}$ with covariance $\mathbf{P}$. In this way, the spread in the ensemble for each element represents the variance of the corresponding element in the state vector.

The ensemble representation of $\mathbf{P}$ is used to approximate two terms of the Kalman gain matrix. In this way, $\mathbf{K}$ - and hence updates of the state vector and covariance matrix - is computed more efficiently. The approximations in the EnKF are:

$$\mathbf{H}\mathbf{P}\mathbf{H}^{\mathrm{T}} \approx \frac{1}{N-1}\left(\mathcal{H}(\mathbf{x}'_1), \mathcal{H}(\mathbf{x}'_2), \ldots, \mathcal{H}(\mathbf{x}'_N)\right)\left(\mathcal{H}(\mathbf{x}'_1), \mathcal{H}(\mathbf{x}'_2), \ldots, \mathcal{H}(\mathbf{x}'_N)\right)^{\mathrm{T}}, \tag{2.14}$$

and

$$\mathbf{P}\mathbf{H}^{\mathrm{T}} \approx \frac{1}{N-1}\left(\mathbf{x}'_1, \mathbf{x}'_2, \ldots, \mathbf{x}'_N\right)\left(\mathcal{H}(\mathbf{x}'_1), \mathcal{H}(\mathbf{x}'_2), \ldots, \mathcal{H}(\mathbf{x}'_N)\right)^{\mathrm{T}}. \tag{2.15}$$

Note that the linearized operator $\mathbf{H}$ is no longer needed in the calculations, since its place is taken by the actual transport model $\mathcal{H}$. This in itself is an advantage of the EnKF, but moreover allows the use of non-linear transport models.

Once the Kalman gain matrix is obtained, the state vector and covariance matrix are updated according to (2.4) and (2.6). The ensemble of state vector members is updated as well:

$$\mathbf{x}'_{\mathbf{opt},i} = \mathbf{x}'_{\mathbf{0},i} - \tilde{\mathbf{k}}\mathcal{H}(\mathbf{x}'_{\mathbf{0},i}). \tag{2.16}$$

Here, $\mathbf{x}'_{\mathbf{0},i}$ are the prior ensemble members, and $\mathbf{x}'_{\mathbf{opt},i}$ the ensemble members after optimization, for $i = 1, \ldots, N$. The vector $\tilde{\mathbf{k}}$ $[m \times 1]$ is the product of $\mathbf{K}$ and a scalar:

$$\tilde{\mathbf{k}} = \mathbf{K} \cdot \left(1 + \sqrt{\frac{\mathbf{R}}{\mathbf{H}\mathbf{P}_\mathbf{0}\mathbf{H}^{\mathrm{T}} + \mathbf{R}}}\right)^{-1} \tag{2.17}$$

After all previously explained steps, one arrives with an updated state vector, ensemble of state vectors, and covariance matrix. With the first, corresponding concentration distributions can be calculated with the transport model. However, following this straightforward procedure, is rather expensive for many observations, since the transport model has to run many times. Actually, concentrations should be sampled at the places and times of the observations (in order to compare them later on), and this is more easily done with the following calculations (performed for each observation ($i = 1, \ldots, n$)):

$$\mathcal{H}(\mathbf{x_{opt}})_i = \mathcal{H}(\mathbf{x_0})_i + \mathbf{H}_i\mathbf{K}(\mathbf{y} - \mathcal{H}(\mathbf{x_0})), \tag{2.18}$$

for the updated state vector. And for the updated ensemble of state vectors:

$$\mathcal{H}(\mathbf{x'_{opt}})_i = \mathcal{H}(\mathbf{x'_0})_i - \mathbf{H}_i\tilde{\mathbf{k}}\mathcal{H}(\mathbf{x'_0}). \tag{2.19}$$

From (2.18) and (2.19) it seems as if the linearized operator is used to sample the modeled concentrations, but this is not the case. For both equations, only the product of $\mathbf{H}$ and $\mathbf{K}$ (recall that $\tilde{\mathbf{k}}$ is a product of $\mathbf{K}$ and a scalar) is calculated. Actually, the product of $\mathbf{H}$ with the first term of $\mathbf{K}$, '$\mathbf{PH}^{\mathrm{T}}$', is approximated as before in (2.14). The other terms are known from previous steps in the analysis.

As shown above, the Ensemble Kalman Filter combines knowledge on observations and a priori estimates to optimize a state vector. The state vector parameters can describe multiple processes, as is illustrated in the experiment of Chapter 4. They determine, via the transport model, the distribution of trace gas concentrations. The optimized concentrations are sampled at locations and times where observations are available. Comparing these values is useful to assess the quality of the transport model and/or the update of the state vector parameters.

Chapter 3

A simplified transport model: explanation and implementation

As stated in the first objective of this study, we assess the performance of CTDAS in optimizing parameters of a transport model, and the aim of this research is to do this for the transport model TM5. However, to get a first understanding of the Ensemble Kalman Filter in relation to optimizing tracer transport, we design a simplified transport model. Section 1 presents a brief overview of the processes included in the model. Furthermore, it describes how these processes are implemented numerically, and gives special attention to the numerical scheme and stability issues. Section 2 evaluates Peclet number analysis and a realistic scenario, in order to set up 'default settings'. These settings assure that all relevant processes - that are contained in the simplified model - contribute to the evolution of the concentration profile, and can be assessed in the experiment later on in Chapter 4.

1 Implementation

Section 1.1 discusses the processes that we include in the simplified transport model. Section 1.2 explains the numerical scheme, and Section 1.3 presents a time step criterion to assure stable numerics.

1.1 Relevant processes

Like with TM5, the simplified transport model transports concentrations of a trace gas, such as CO_2 or SF_6, through the atmosphere over specified time periods. However, the atmosphere is a one-dimensional concentration field. The base concentration w of the tracer evolves in time because of the following processes:

- advection: a wind is blowing through the domain carrying the tracer on its way. The value of the advection coefficient u represents the strength of the wind, the sign its direction. Since we are dealing with a one-dimensional domain the wind can blow two ways: to the left (u is negative) and to the right (u is positive).

- diffusion: due to concentration differences within the domain, tracer is moved from high to low concentrations. The strength of this transport is modeled by the diffusion coefficient D. Throughout this report, with ‘diffusion’ we do not refer to molecular diffusion, since this is a very slow process, but to transport of tracer that is sub grid scale and hence unresolved by the model. One can think of transport in convective cells or transport by turbulent motions.

- sources and sinks: sources emit amounts of tracer - increasing its concentration in the atmosphere -, whereas sinks take it up - decreasing the concentration. The transport model contains two sources and/or sinks, of which the strength is determined by s_1 and s_2. If s_i is positive, a source is represented, for s_i negative, a sink instead.

These processes are the input parameters of the transport model, and contained in the state vector ($\mathbf{x} = (w, u, D, s_1, s_2)$). It defines the transport and resulting concentration distribution of the tracer.

1.2 Numerical scheme(s)

The advection-diffusion equation, including sources and/or sinks, for a one dimensional space domain is described by:

$$c_t + u \cdot c_x = D \cdot c_{xx} + S. \tag{3.1}$$

Here, c_t represents the change of concentration in time. The advection term is given by the wind speed u multiplied by the change of concentration in space, c_x. Diffusion is represented by the product of the diffusion coefficient D and the second derivative of the concentration w.r.t. space: c_{xx}. Finally, the sources and/or sinks are represented by S. Concentrations (c) are in $mol \cdot m^{-3}$. Assuming a fixed volume (atmosphere) the units of u, D, and S are ms^{-1}, m^2s^{-1}, and $mol \cdot m^{-3}s^{-1}$, respectively.

We discretize equation (3.1) by a forward difference in time, a first order upwind scheme in space, and a second order central difference scheme in space for the first three terms of equation (3.1). Assuming that C_j^n is the concentration at node j at time step n, we have:

$$\begin{aligned} &\tfrac{C_j^{n+1} - C_j^n}{\Delta t} + u \tfrac{C_{j+1}^n - C_j^n}{\Delta x} = D \tfrac{C_{j+1}^n - 2C_j^n + C_{j-1}^n}{(\Delta x)^2} + S_j \quad \text{if } u \geq 0; \\ &\tfrac{C^{n+1} - C^n}{\Delta t} + u \tfrac{C_j^n - C_{j-1}^n}{\Delta x} = D \tfrac{C_{j+1}^n - 2C_j^n + C_{j-1}^n}{(\Delta x)^2} + S_j \quad \text{if } u < 0. \end{aligned} \tag{3.2}$$

Rewriting the above equations results in the following concentration update, that is applied each at time step:

$$C_j^{n+1} = \begin{cases} C_j^n - u \cdot \nu_1 \cdot (C_j^n - C_{j-1}^n) + D \cdot \nu_2 \cdot (C_{j+1}^n - 2C_j^n + C_{j-1}^n) + S_j & \text{if } u \geq 0; \\ C_j^n - u \cdot \nu_1 \cdot (C_{j+1}^n - C_j^n) + D \cdot \nu_2 \cdot (C_{j+1}^n - 2C_j^n + C_{j-1}^n) + S_j & \text{if } u < 0. \end{cases} \tag{3.3}$$

For convenience we use $\nu_1 = \frac{\Delta t}{\Delta x}$ and $\nu_2 = \frac{\Delta t}{(\Delta x)^2}$.

Note that the concentration update at node j not only requires the current concentration at this node, but the value at node $j-1$ and $j+1$ as well. We define periodic boundaries by assuming Dirichlet boundary conditions:

$$c(0, t) = c(L, t) \quad \forall t, \tag{3.4}$$

and:

$$c_x(0,t) = c_x(L,t) \quad \forall t. \tag{3.5}$$

Hence, the first, but also higher, order derivatives at the boundaries are smooth. Now, for $nx+1$ nodes (starting from node 0 up to node nx) we have $C_0 = C_{nx}$, and thus $C_{-1} = C_{nx-1}$, and $C_1 = C_{nx+1}$. Periodic boundaries close the system and concentrations can flow smoothly through the domain. This is suitable for the experiment of Chapter 4, since there we do not want concentrations to rebound from the boundaries of the domain.

1.3 Stability criterion

To assure stability of the numerical scheme, an appropriate time step needs to be determined for each grid size. We apply the Fourier method that defines:

$$C_j^n = \lambda^n \exp(ikj\Delta x), \tag{3.6}$$

with C_j^n the concentration at node j at time step n, k any value, and λ the 'amplification factor' such that $C_j^{n+1} = \lambda C_j^n$ (Morton and Mayers, 2005). We substitute (3.6) in (3.3) and obtain:

$$\lambda(k) = \begin{cases} 1 - (u \cdot \nu_1 + 2D \cdot \nu_2)\,(1 - \cos(k\Delta x)) + u \cdot \nu_1 \cdot i \sin(k\Delta x) & \text{if } u \geq 0; \\ 1 + (u \cdot \nu_1 - 2D \cdot \nu_2)\,(1 - \cos(k\Delta x)) + u \cdot \nu_1 \cdot i \sin(k\Delta x) & \text{if } u < 0. \end{cases} \tag{3.7}$$

We leave out the term S_j since it does not affect the stability of the scheme. Note that ν_1 and ν_2 are the same as before.

For stability, we require:

$$|\lambda(k)^n| \leq K, \quad \text{for} \quad n\Delta t \leq t_F, \forall k, \tag{3.8}$$

which assures that the growth in a finite time (t_F) is bounded. We test $|\lambda(k)| < 1$ for any value of k to assure that the concentration at node j converges in time. Analysis on (3.7) provides constraints on the time step such that the stability condition is satisfied:

$$\Delta t < \frac{(\Delta x)^2}{2D + u\Delta x} \quad \text{if } u \geq 0, \tag{3.9}$$

and for the opposite wind direction:

$$\Delta t < \frac{(\Delta x)^2}{2D - u\Delta x} \quad \text{if } u < 0. \tag{3.10}$$

2 Default settings

Section 2.1 briefly discusses how to use the Peclet number as a measure for relative contribution of advection and diffusion in the simplified transport model. Section 2.2 evaluates a realistic example of a system with advection, diffusion and sources and/or sinks. In Section 2.3 we determine, on basis of this scenario, appropriate default settings that are used and examined in the experiment in Chapter 4.

2.1 Peclet analysis

To determine the relative contribution of advection and diffusion on concentrations of a certain tracer, we scale the relevant terms of equation (3.1). For advection we find:

$$u\frac{\delta c}{\delta x} \sim U\frac{C}{L},$$

and for diffusion:

$$D\frac{\delta c}{\delta x^2} \sim D\frac{C}{L^2}.$$

Here, C is a typical concentration value, L the approximate domain length, U a typical value for wind speed, and D for tracer transport. The ratio of advection and diffusion is determined:

$$\frac{\text{advection}}{\text{diffusion}} = \frac{U \cdot C/L}{D \cdot C/L^2} = \frac{U \cdot L}{D}. \tag{3.11}$$

The ratio of (3.11) is known as the Peclet number, Pe. If one finds $Pe \gg 1$ (or $Pe > 10$) the contribution of advection on the concentration field is larger than the contribution of diffusion, which can therefore be neglected. Vice versa, diffusion is the dominant process for $Pe \ll 1$ (or $Pe < 0.1$), and advection may be neglected. For the experiment in Chapter 4 we need a more or less equal contribution of advection and diffusion, and we aim for a Peclet number close or equal to 1.

2.2 A realistic scenario

Figure 3.1 illustrates a realistic scenario, containing advection, diffusion, and sources and sinks of CO_2, that can be simulated with the transport model. In the model, two source/sink terms are allowed: s_1 and s_2. Let's assume that the first one is a source of CO_2, represented by a factory, and the other one a sink, represented by a forest. The factory and the forest are 5 km apart. Due to the periodic boundaries of our system, this 5 km distance occurs on both sides of the source and sink. Hence the total length of the domain is 10 km: $L = 1.0\text{e}4$ m. Assuming that the domain is located in the Netherlands, we obtain an annual mean wind speed of 3-4 ms^{-1} (Yin, 2000). Furthermore, we assume a wind that carries CO_2 along from the left to the right of the domain with a constant velocity scale of $U = 3.0$ ms^{-1}. Lastly, turbulent motions cause mixing of relatively high CO_2 concentrations around the factory with low concentrations around the forest. Pisso et al. (2009) determine turbulent diffusion coefficients in the free troposphere. For the horizontal direction they find $D_h = 1.0\text{e}4$ m^2s^{-1}, which we use for D.

To see whether in this case both advection and diffusion are important for the distribution of CO_2 concentrations, we calculate the Peclet number:

$$Pe = \frac{3.0\ ms^{-1} \cdot 1.0e4\ m}{1.0\text{e}4\ m^2s^{-1}} = 3.0.$$

Recall from Section 2.1 that $0.1 < Pe < 10$ indicates that neither advection, nor diffusion is dominating, and that a Peclet number around 3.0 is suitable (for our later experiment) to represent the realistic scenario as explained above.

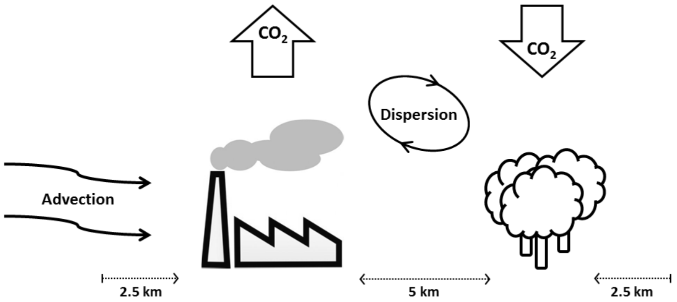

Figure 3.1: An example case of a source (factory) emitting CO_2 and a sink (forest) taking up CO_2. Concentrations are affected by a wind (advection), blowing from left to right through the domain, and turbulent mixing of tracer (dispersion).

2.3 Setup test experiment

The next step is to convert the realistic scenario of the previous section into settings for our test experiment in the next chapter. We consider the Peclet number, and require a balance between the domain length, advection, and diffusion such that $x \cdot u/D = 3.0$. Furthermore, we place the source and sink in accordance with Section 2.2. Finally, we determine an appropriate run time and time step.

The domain is set to $x = [0, 1]$, division into 50 intervals gives $\Delta x = 0.02$. Considering that $Pe = 3.0$, we set $u = 3.0$ and $D = 1.0$. We want the source and sink to contribute to the concentration changes as well and therefore we have $s_1 = 0.1$, and $s_2 = -0.1$. They have equal magnitude, but opposite sign. Recall that the source adds concentration at each time step and therefore is positive. Vice versa for the sink. Important to mention is that we neglect the eventual effect of CO_2 fertilization, that would prescribe the sink to take up more CO_2 if more is available. In our model we assume the uptake by the sink is not dependent on the concentration. The source and sink are placed at $x = 0.25$ and $x = 0.75$ respectively. Note that in both directions, the source and sink are 0.5 apart, which is comparable to the realistic scenario. For the base concentration we may choose any value since we are not interested in the magnitude of concentrations, but in its change driven by advection, diffusion, and sources and sinks. The simplified transport model does not preserve positive concentrations (whereas TM5 does). To avoid negative concentrations we choose a value fairly greater than zero: $w = 10.0$.

In short, we define the following values for the state vector:

$$\mathbf{x} = (10.0, 3.0, 1.0, 0.1, -0.1), \tag{3.12}$$

and refer to this as the ‘default settings’.

Finally, an appropriate run time and time step for the experiment need to be determined. By the method of separation of variables for partial differential equations and dimensional analysis of (3.1) we find that $t_0 = 0.0$ and $t_{end} = 0.1$ are appropriate to capture the exponential decay, caused by diffusion, without reaching the steady state too early in the experiment. This avoids that concentrations at a fixed location remain constant throughout the experiment. The derivation of t_0 and t_{end} is elaborated in Appendix A. Here, we infer an appropriate time step of $\Delta t = 1.0e\text{-}4$ from restriction (3.9) and the settings of (3.12).

Figure 3.2 displays evolution in time of the concentration profile for the default settings. The source and sink are visible, as are their advected and collapsing plumes. To illustrate the influence of transport by diffusion on the concentration profile, we observe cases for a relatively low and high D - representing weak and strong mixing respectively. Resulting Figures 3.3(a) and 3.3(b) show that weak mixing causes stronger gradients over the domain, and that the opposite is true for strong mixing.

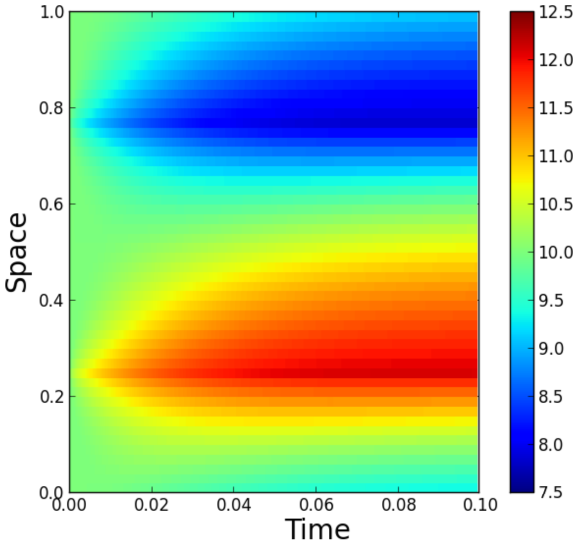

Figure 3.2: Concentration in time for a source ($s_1 = 0.1$) at $x = 0.25$ and a sink ($s_2 = -0.1$) at $x = 0.75$ for the 'default' diffusion coefficient $D = 1.0$.

To summarize, we implement a simplified transport model according to the advection-diffusion equation in (3.1). It calculates the distribution of a tracer's concentrations over a one-dimensional domain with periodic boundaries, depending on a base concentration (w), advection (u), diffusion (D), and a source (s_1) and a sink (s_2). Based on Peclet analysis, and a realistic scenario, we determined default settings. These are suitable to examine the influence of diffusion properties in the transport model on (flux) estimates, obtained by a data-assimilation system. In Chapter 4, we elaborate on this experiment.

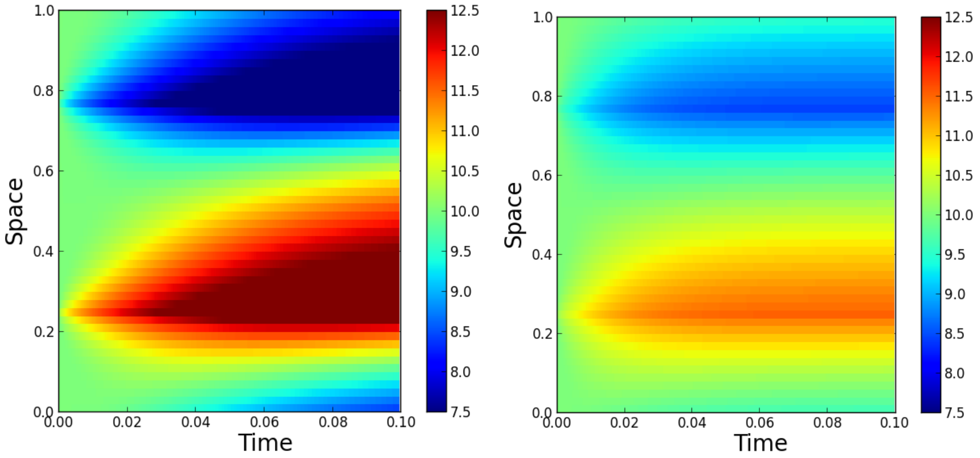

(a) $D = 0.5$ (b) $D = 1.5$

Figure 3.3: Concentration in time for a source ($s_1 = 0.1$) at $x = 0.25$ and a sink ($s_2 = -0.1$) at $x = 0.75$ for a small and a large diffusion coefficient D.

Chapter 4

A data-assimilation test experiment

By combining the Ensemble Kalman Filter and the simplified transport model of the previous chapter, we define our so-called ‘toy-model’. With the toy-model, we aim to obtain insight in optimizing (transport) parameters of a transport model with the CTDAS procedure, and hence optimize (some of the) state vector parameters of the transport model: $\mathbf{x} = (w, u, D, s_1, s_2)$. Recall from Chapter 3 that these represent the base concentration, advection, diffusion, a first source or sink, and a second source or sink of tracer, respectively.

This chapter discusses the results of the experiment with the toy-model. In line with CO_2 flux estimations using TM5, we first estimate the source and sink strength (s_1 and s_2) with the toy-model. Section 1 shows that this results in good, but highly correlated, estimated fluxes. In Section 2, we mimic errors/biases in transport properties of transport models, as discussed by Stephens et al. (2007), by estimating fluxes as before, but using incorrect diffusion coefficients. Significant under- and overestimations of the fluxes illustrate the importance of correct tracer transport. Finally, to solve the problem of Section 2, we optimize the three relevant parameters (diffusion, the source, and the sink) at the same time. Section 3 identifies that this does not necessarily lead to improved transport properties.

Every section is divided in two parts: the data-assimilation with one measurement station (tested at three different locations) is followed by the optimization with an observational network.

We assure that sufficient accuracy of the results is guaranteed by using 20 observations and 100 ensemble members in all optimizations in this chapter. This is necessary to estimate one to five parameters. Furthermore, we verified that the toy-model works properly for two simplified cases. In the first, we observe that parameters of which the covariance is set to nearly zero ($1.0e\text{-}7$), stay fixed during the optimization, as they should. Note that the covariance never can be exactly zero. This would make P a singular matrix, which is problematic for in the EnKF (see equation(2.2)). Second, we verify that the model is able to estimate one parameter at a time, even when its a priori estimate deviates significantly from the true value.

1 Estimating the source and sink parameters

This section discusses the estimation of the two flux parameters: a source s_1 and a sink s_2. We did not estimate w, u, or D for different reasons. The concentration of tracers, such as CO_2 and SF_6, is conserved in the atmosphere and should not be changed unless the effect is explained by the influence of a source or sink. Hence, w should not be estimated. Optimizing advection is not an option as well. In the toy-model we assume a constant wind, but in reality advection changes over time. Transport models are fed with meteorological data every few hours to represent accurate conditions, and optimization of u could violate these circulation patterns. We do optimize D, but this is examined later in Section 3. Hence, the base concentration, advection and diffusion are fixed to the default values as determined in Section 2.3 of Chapter 3. Table 4.1 displays the corresponding settings.

Table 4.1: Settings to test assimilation of both s_1 and s_2. Other parameters are fixed to their default values. Note that P_{ii} represent the covariances - actually variances, since they are placed on the diagonal of P - belonging to parameter $i = 1$ to 5.

	$w\ \left[\frac{mol}{m^3}\right]$	$u\ \left[\frac{m}{s}\right]$	$D\ \left[\frac{m^2}{s}\right]$	$s_1\ \left[\frac{mol}{m^3 \cdot s}\right]$	$s_2\ \left[\frac{mol}{m^3 \cdot s}\right]$
real values	10.0	3.0	1.0	0.1	-0.1
a priori values	10.0	3.0	1.0	0.0	0.0
P_{ii}	1.0e-7	1.0e-7	1.0e-7	0.04	0.04

1.1 One measurement station

The optimization of s_1 and s_2 with one measurement station is performed at three locations in the domain: one on the right side of the source ($x = 0.4$), another around the middle of the domain ($x = 0.6$), and the last one close to the sink ($x = 0.8$). The first station is mainly affected by the source, the last by the sink and the middle station not much by either of them. Namely, this station is located relatively far away from the source, and at the same time on the left side of the sink. Concentrations carried by advection first pass the station before reaching the sink, such that its influence can hardly be measured. Table 4.2 displays the results.

Table 4.2: Results for optimization of s_1 and s_2, with r the correlation coefficient of $s_{1,opt}$ and $s_{2,opt}$, RMSD is the root mean squared difference (RMSD) between model and observations, and J is the cost function.

station(s)	$s_{1,0} = s_{2,0}$	$s_{1,opt}$	$s_{2,opt}$	r	RMSD$_0$	RMSD$_{opt}$	J_0	J_{opt}
$x = 0.4$	0.0 ± 0.2	0.10 ± 0.01	-0.10 ± 0.01	-0.96	25.1	0.002	2514	0.7
$x = 0.6$	0.0 ± 0.2	0.10 ± 0.02	-0.10 ± 0.01	-0.99	1.3	0.004	126	0.9
$x = 0.8$	0.0 ± 0.2	0.10 ± 0.01	-0.10 ± 0.00	-0.91	59.5	0.001	5946	0.6
random	0.0 ± 0.2	0.10 ± 0.00	-0.10 ± 0.00	-0.67	23.8	0.001	2377	0.6

We find accurate estimates of s_1 and s_2 for all three measurement stations. In fact, this is not surprising since we use the correct base concentration, advection and diffusion in the transport model. The location of the measurement stations - and their proximity to either the source or sink - did not affect the results.

Furthermore, we find a strong negative correlation between $s_{1,opt}$ and $s_{2,opt}$. This makes sense, since increasing (strengthening) the source leads to higher concentrations, and hence a decrease (strengthening) of the sink is needed to match observations.

Finally, we find that both the root mean squared difference (RMSD) between model and observations and the cost function decrease significantly by the optimization, which means that the new solution improved compared to the prior. We observe this in all further runs in the experiment, and so we show only the optimized values of RMSD and J from here on.

1.2 An observational network

From the results in Table 4.2 we see that the flux estimates using an observational network (20 observations at random locations in the domain) are accurate, and comparable to single station estimates. Different is the correlation between $s_{1,opt}$ and $s_{2,opt}$, which is significantly lower for the network. Hence, by including observations at many locations, the estimate for either the source or sink is less constrained by the estimate of the other one. Overall, we conclude that the toy-model is well able to estimate fluxes of tracer if it knows the true values of the base concentration, wind speed, and diffusion coefficient. Also, a sufficient amount of observations is required.

2 The influence of unresolved transport

As mentioned before, transport properties are of main importance when estimating fluxes of CO_2. Differences in transport between the models result in biases in flux estimates (Stephens et al., 2007), which are not desirable. With the toy-model we address this problem of inaccurate transport and how it affects the flux estimates by optimizing s_1 and s_2 as before, but now feed the toy-model with a diffusion coefficient D_0 that is different from the real value. We distinguish between two cases: too little transport of tracer (case 1: $D_0 = 0.5$, see also Figure 3.3(a)) and too strong transport (case 2: $D_0 = 1.5$, see also Figure 3.3(b)). One has to keep in mind that the diffusion examined in the toy-model includes horizontal transport only.

Settings used for this experiment are equal to the ones in Table 4.1, only the a priori values of D are 0.5 and 1.5 for case 1 and 2, respectively.

2.1 One measurement station

Table 4.3 presents the results of testing the influence of inaccurate transport.

It is clear that the estimates of s_1 and s_2 are not accurate and that the prescribed uncertainty range is often not enough to capture the real solution. Keep in mind, that the values of s_1 and s_2 are added to the concentrations at $x = 0.25$ and $x = 0.75$, respectively, at each time step. Considering 1000 time steps ($t_{end} = 0.1s$ and $\Delta t = 1.0\text{e}{-4}s$), an error of $0.01\frac{mol}{m^3 \cdot s}$ in the estimates results in a total concentration deviation of $10\frac{mol}{m^3 \cdot s}$.

In this case, the errors are dependent on the location of the measurement station. Too weak diffusion in the model causes that concentrations are less mixed over the domain, and that the concentration profile shows stronger gradients than the profile of observations. At the station close to the source ($x = 0.4$) too high concentrations, compared to observations, are found by the model. To match the observations, the

Table 4.3: Results for optimization of s_1 and s_2 with too weak tracer transport (case 1: $D_0 = 0.5$) and too strong transport (case 2: $D_0 = 1.5$). Here, r is the correlation coefficient of $s_{1,opt}$ and $s_{2,opt}$, RMSD is the root mean squared difference between model and observations, and J is the cost function. Note that for the last two, only the optimized values are shown.

	station(s)	$s_{1,0}= s_{2,0}$	$s_{1,opt}$	$s_{2,opt}$	r	RMSD$_{opt}$	J_{opt}
case 1	$x = 0.4$	0.0 ± 0.2	0.07 ± 0.00	-0.15 ± 0.02	-0.93	0.12	13.1
	$x = 0.6$	0.0 ± 0.2	0.07 ± 0.02	-0.09 ± 0.02	-0.99	0.02	2.7
	$x = 0.8$	0.0 ± 0.2	0.12 ± 0.01	-0.07 ± 0.00	-0.86	0.08	8.2
	random	0.0 ± 0.2	0.06 ± 0.00	-0.07 ± 0.00	-0.41	0.64	64.3
case 2	$x = 0.4$	0.0 ± 0.2	0.12 ± 0.01	-0.09 ± 0.02	-0.98	0.02	2.6
	$x = 0.6$	0.0 ± 0.2	0.12 ± 0.02	-0.11 ± 0.02	-0.99	0.01	1.6
	$x = 0.8$	0.0 ± 0.2	0.10 ± 0.01	-0.13 ± 0.00	-0.93	0.03	4.1
	random	0.0 ± 0.2	0.14 ± 0.00	-0.14 ± 0.00	-0.81	0.22	23.1

model can do two things. First, underestimating the source and overestimating the sink to bring concentrations at $x = 0.4$ to a lower level. And second, underestimating the source and underestimating the sink (this is prescribed by the negative correlation between $s_{1,opt}$ and $s_{2,opt}$[1].). Which of the two properties is preferred by the toy-model follows from the strength of the correlation coefficient. Strong (negative) correlations (see for instance $x = 0.6$) are in favor of the last effect, and give little freedom for the sink to amplify, because the source does not. On the other hand, for weaker correlations ($x = 0.4/x = 0.8$) the strength of s_2/s_1 is overestimated - even though s_1/s_2 is underestimated - to bring concentrations at the specific stations down/up. The opposite occurs for strong diffusion.

Most important, we learn that wrong transport properties lead to wrong source and sink estimates.

2.2 An observational network

The bias in flux estimations caused by inaccurate transport cannot be overcome by the use of an observational network. However, from the results in Table 4.3 we obtain that the errors of single measurement stations reduce. For instance, increasing the sink strength in order to lower concentrations at $x = 0.4$ is not an option, since measurements around the sink are available. This results in equally estimated source and sink strengths, even though their correlation is smaller than found in Section 2.1.

It stands out that for too weak diffusion, the model underestimates both the source and sink, whereas these are overestimated for too strong diffusion. Considering that low/high diffusion results in stronger/weaker concentration gradients than in observations, it is logical that s_1 and s_2 are under/overestimated.

Overall, we conclude that correct transport properties in the model are essential to obtain accurate source and sink strengths.

---

[1] See Section 1.1.

3 Estimating the source, the sink, and the transport parameters

The exact settings to represent sub grid transport processes in reality are unknown. Fixing them to a certain (possibly wrong) value is not a good option, as is illustrated in the previous section. A possible solution is to optimize not only the fluxes (s_1 and s_2) but the transport by diffusion (D) as well:

Table 4.4: Settings to test assimilation of both D, s_1, and s_2. Other parameters are fixed to their default values. Note that P_{ii} represent the covariances - actually variances, since they are placed on the diagonal of P - belonging to parameter $i = 1$ to 5.

	w $\left[\frac{mol}{m^3}\right]$	u $\left[\frac{m}{s}\right]$	D $\left[\frac{m^2}{s}\right]$	s_1 $\left[\frac{mol}{m^3 \cdot s}\right]$	s_2 $\left[\frac{mol}{m^3 \cdot s}\right]$
real values	10.0	3.0	1.0	0.1	-0.1
a priori values	10.0	3.0	1.25	0.0	0.0
P_{ii}	1.0e-7	1.0e-7	0.0625	0.04	0.04

3.1 One measurement station

Table 4.5 displays the results of the optimized source, sink, and transport parameters.

Table 4.5: Results for optimization of s_1, s_2, and D. J_{opt} is the optimized cost function. Its value is directly related with RMSD$_{opt}$, that therefore is not shown.

station(s)	D_0	D_{opt}	$s_{1,0} = s_{2,0}$	$s_{1,opt}$	$s_{2,opt}$	J_{opt}
$x = 0.4$	1.25 ± 0.25	1.28 ± 0.25	0.0 ± 0.2	0.10 ± 0.01	-0.11 ± 0.03	72.2
$x = 0.6$	1.25 ± 0.25	1.29 ± 0.23	0.0 ± 0.2	0.10 ± 0.03	-0.10 ± 0.02	1.4
$x = 0.8$	1.25 ± 0.25	1.25 ± 0.24	0.0 ± 0.2	0.10 ± 0.01	-0.11 ± 0.01	38.7
random	1.25 ± 0.25	1.28 ± 0.23	0.0 ± 0.2	0.10 ± 0.01	-0.10 ± 0.01	78.9

From the results, we see that optimizing both D, s_1, and s_2 at the same time is not suitable to test diffusion properties. The optimization is successful in the sense that the simulated concentrations are improved by the assimilation (Figure 4.1 illustrates this for the observational network, but also for single measurement stations the concentration field improves). This is caused by the estimations of s_1 and s_2, that are accurate and contain the real solution within the uncertainty range. However, optimized diffusion values hardly change compared to the prior, as does the uncertainty range. This suggest that the diffusion parameter does not gain information from the optimization, and that the system prefers to match observations by adjusting the source and sink. Hence, it is difficult to examine transport properties (diffusion) in an experiment where it is optimized together with the fluxes (source/sink).

3.2 An observational network

From Table 4.5 it is evident that the estimations, using an observational network, are comparable to the ones of single stations. Figure 4.1 shows that indeed the optimization improves the match with observations compared to the prior. However, the use of the an observational network can not prevent that the optimization is dominated by adjustments to the fluxes. Especially if the true values of D, s_1, and s_2 are unknown, it is difficult to verify whether the optimization improves the transport property, or that its combination with specific source and sink strengths is the best way to match observations.

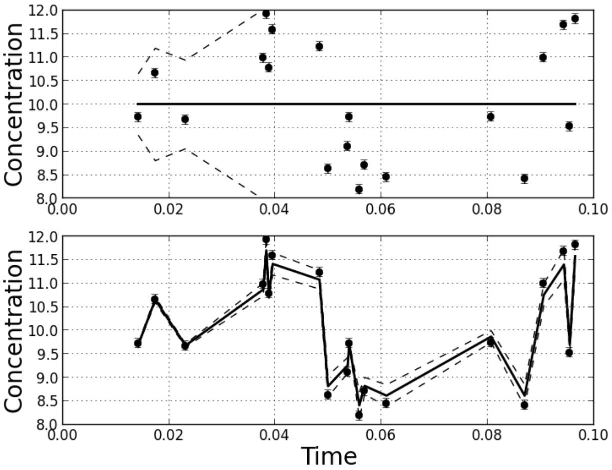

Figure 4.1: Modeled (solid line) and observed (black dots) concentrations with prior parameter values and optimized parameter values in the top and bottom figure, respectively. The dashed lines indicate the standard deviation of the simulated ensemble members ($\mathcal{H}(\mathbf{x}')$). The error bars on the dots illustrate the uncertainty of the observations (also known as 'model-data-mismatch'). Multiple stations are used such that the profile is not as smooth as it would be for a single station.

To conclude, improved transport properties in tracer transport models should be obtained by solely optimizing this process. Hence, the magnitude and distribution of sources and sinks in the domain need to be known. Since CO_2 is not a suitable tracer in this respect, we switch to another tracer: SF_6. How we assess transport properties in TM5 using SF_6 is discussed in the next chapters.

Chapter 5

Transport in TM5

From the simplified transport model of the toy-model, we now switch to TM5. Section 1 provides a brief introduction to the model. Section 2 and 3 explain the main properties the advection and convection routine, respectively. This research focuses on atmospheric transport, and will not examine or discuss the chemistry routine.

1 Main properties

First, special about TM5 is its use of two-way nested zooming. The grid size over a specific region can be refined, and simulations can be performed with higher accuracy in this region. Boundary conditions for the refined (zoom) region are provided by the coarser parent grid. Moreover, this relation works in two ways, since results of the zoom region are communicated back to the parent grid as well (Krol et al., 2005). This research does not use the zooming ability of TM5, and performs all simulations on a (parent) grid of $6° \times 4°$.

Furthermore, TM5 uses offline input data to represent meteorological conditions, such as weather, ocean-wave and land-surface conditions. For this research we use the ERA-Interim (ERA-I) reanalysis data from the European Centre for Medium-Range Weather Forecasts (ECMWF). Dee et al. (2011) state that ERA-I reanalysis provides a *'multivariate, spatially complete, and coherent record of the global atmospheric circulation'* in the form of 3-hourly surface parameters and 6-hourly upper-air parameters (vertical levels represent the the atmosphere up to 0.1 hPa). They further explain that the data represent available observations, match the basic dynamical fields, and are consistent with the laws of physics as well. ERA-I is obtained via data-assimilation with the 4D-Var method, and a forecast model that can extrapolate observed parameters to nearby locations and forward in time (Dee et al., 2011) - as TM5 does for trace gasses. To assure consistency of the data, ERA-I reanalysis data is produced with a single version of the data-assimilation system and forecast model: IFS release Cy31r2, that was used as operational forecasting system at ECMWF from 12 December 2006 until 5 June 2007 (Dee et al., 2011).

To verify that our results do not entirely depend on the choice of the input meteorology data set, we perform simulations with Operational Data (OD) of ECMWF as well. The data is produced via data-assimilation, like ERA-I, but uses the operational IFS releases (most up to date data-assimlation system and forecasting model at the time) instead of one fixed version for the whole data set (Dee et al., 2011). Hence, OD data generally has higher accuracy, but is less consistent than ERA-I data.

Lastly, transport of tracers in the model is calculated via so-called ‘operator splitting’. This means that the relevant processes are separated and performed once in a certain specified order, and a second time in reversed order. The advantage is that no small time steps are needed for the stiff chemistry calculations (Verwer et al., 1999). Processes that are distinguished in TM5 are horizontal (X,Y) and vertical (Z) advection, parameterized vertical transport by deep convection and diffusion (V), and chemistry (C). The order of the calculations in the TM5 parent grid is: XYZVC-CVZYX (Krol et al., 2005).

2 The advection routine

The advection scheme in TM5 we refer to as the ‘slopes scheme’, since it describes tracer mass within each grid box as a mean concentration and a ‘slope’, representing the spatial gradient of concentration in the grid box (Russell and Lerner, 1981). The slopes scheme is used in TM3 (Berkvens et al., 1999), and later on in TM5 as well. In this section, we explain the implementation of slopes in the advection routine based on the papers of Berkvens et al. (1999) and Russell and Lerner (1981).

An illustration of tracer mass in a grid box with the slopes scheme is depicted in the left side of Figure 5.1 (Berkvens et al., 1999). The right hand side shows an upwind scheme, which actually is a version of the slopes scheme with slopes set to zero. Note that the representation of advection is in 1-D, and that the three directions (X, Y, and Z) are calculated similarly and subsequently in TM5. One finds the air mass m, and mixing ratio of tracer χ on the horizontal and vertical axes respectively. The dot represents the average mixing ratio in the grid box, which we will call $\tilde{\chi}$ from here on. The line through the average mixing ratio is characterized by the slope s, and indicates the spatial concentration gradient within the grid box. The linear distribution of mixing ratio in grid box i is formulated by:

$$\chi_i = \tilde{\chi_i} + s_i \cdot m_i \tag{5.1}$$

The total mass of tracer in the grid box is the integral of (5.1). For the upwind scheme this is rather straightforward since the area under the slope is a square, and hence for grid box i we have: area $= m_i \cdot \tilde{\chi_i} = \mu_i$.

The air mass that is transported by advection is denoted by A. As seen from grid box i, air mass $A_{i-1/2}$ is entering the box from the left, and air mass $A_{i+1/2}$ is leaving the grid box on the right side. The time-step update for the total air mass in grid box i is therefore:

$$m_i^{n+1} = m_i^n + A_{i-1/2}^n - A_{i+1/2}^n. \tag{5.2}$$

To obtain the amount of tracer that is transported with this air mass, one needs to determine the area bounded by the slope, the grid box boundary, and $A_{i+1/2}$. Note that only the outgoing flux needs to be determined since the incoming flux of box i is the outgoing flux of box $i-1$. We illustrate the determination of the fluxes by defining three regions (A, B, and C) in grid box i as illustrated in Figure 5.2.

Recall that the total mass of tracer in the grid box is equal to the area under the slopes line. Hence, the outgoing mass flux of tracer is the shaded area in Figure 5.2, which is the sum of regions A and B. The surface of area A is easily calculated:

$$\begin{aligned} A &= A_{i+1/2} \cdot \tilde{\chi_i}; \\ &= A_{i+1/2} \cdot \frac{\mu_i}{m_i}, \end{aligned} \tag{5.3}$$

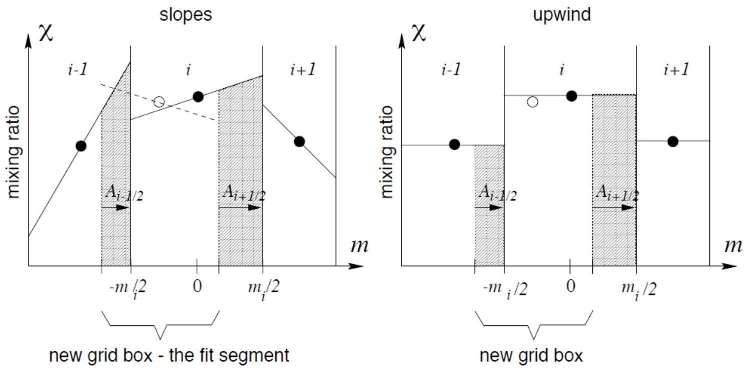

Figure 5.1: The slopes scheme as implemented in TM5. On the horizontal axis is given the total air mass m, on the vertical axis the mixing ratio of tracer χ. The dots represent the average mixing ratio in the grid box ($\tilde{\chi}$), the line through it represents the slope s_i, i.e. the spatial concentration gradient within the box. The advected air masses are given by $A_{i-1/2}$ and $A_{i+1/2}$. The open dot and dashed line are the mean mixing ratio and slope at the next time step, respectively. The figure is taken from Berkvens et al. (1999).

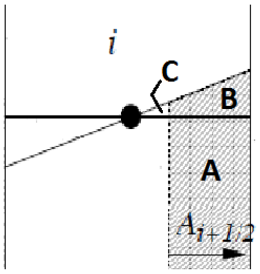

Figure 5.2: Zoomed-in view of Figure 5.1 of grid box i. Note that the solid line is added to this figure to represent the upwind scheme (with zero slopes). The area that indicates the outgoing flux of tracer mass is the sum of the areas A and B.

with $A_{i+1/2}$, $\tilde{\chi}_i$, μ_i, and m_i as indicated above. To obtain the surface of B, we first determine the surface of B+C and then subtract the area of C. For the combined areas we find:

$$\begin{aligned} B + C &= \tfrac{1}{2} \cdot \tfrac{1}{2} m_i \cdot \tfrac{1}{2} m_i s_i; \\ &= \tfrac{1}{8} m_i^2 s_i. \end{aligned} \tag{5.4}$$

And for the area of C:

$$\begin{aligned} C &= \tfrac{1}{2} \cdot (\tfrac{1}{2} m_i - A_{i+1/2}) \cdot (\tfrac{1}{2} m_i - A_{i+1/2}) s_i; \\ &= \tfrac{1}{8} m_i^2 s_i - \tfrac{1}{2} m_i A_{i+1/2} s_i + \tfrac{1}{2} A_{i+1/2}^2 s_i. \end{aligned} \tag{5.5}$$

The mass flux of tracer in box i follows by summing the area of A and B, so calculate $A + (B + C) - C$ from equations (5.3), (5.4), and (5.5). We define $\sigma_i = \frac{1}{2} s_i m_i^2$, since it is stored this way in the array `rxm` in TM5[1]. By changing `rxm`, the slopes, and

---

[1] Note that this statement in (Berkvens et al., 1999) is written as $\sigma_i = \frac{1}{2} s_i m_i$, but that this must

hence the spatial gradients in the model can be adjusted. This leads to the following update for the outgoing tracer mass flux at each time step:

$$F^n_{i+1/2} = \begin{cases} \frac{A^n_{i+1/2}}{m^n_i}\left(\mu^n_i + \left(1 - \frac{A^n_{i+1/2}}{m^n_i}\right)\sigma^n_i\right) & \text{if } A^n_{i+1/2} \geq 0; \\ \frac{A^n_{i+1/2}}{m^n_{i+1}}\left(\mu^n_{i+1} - \left(1 + \frac{A^n_{i+1/2}}{m^n_{i+1}}\right)\sigma^n_{i+1}\right) & \text{if } A^n_{i+1/2} < 0. \end{cases} \tag{5.6}$$

Using the tracer mass flux of (5.6), update for the tracer mass at each time step is given by:

$$\mu^{n+1}_i = \mu^n_i + F^n_{i-1/2} - F^n_{i+1/2}. \tag{5.7}$$

The tracer mass of a grid box is stored in the array `rm` in TM5.

Lastly, the slopes are updated. The new slope is calculated by a least squares fit of the old slopes in the domain $[-\frac{1}{2}m_i - A_{i-1/2}, \frac{1}{2}m_i - A_{i+1/2}]$. Note that the 'old' slope in this domain is a piecewise linear function, since the domain includes two grid boxes:

$$f(m) = \begin{cases} \tilde{\chi}^n_i + s^n_{i-1} \cdot m & \text{for } -\frac{1}{2}m_i - A_{i-1/2} \leq m < -\frac{1}{2}m_i; \\ \tilde{\chi}^n_{i+1} + s^n_i \cdot m & \text{for } -\frac{1}{2}m_i \leq m \leq \frac{1}{2}m_i - A_{i+1/2}. \end{cases} \tag{5.8}$$

In Figure 5.1, the updated slope is shown as the dashed line. Note that it intersects the updated average mixing ratio, which is represented by the open dot. The update for the slopes at each time step is:

$$\begin{aligned} \sigma^{n+1}_i = \sigma^n_i + \frac{1}{m^{n+1}_i} \cdot \quad & \Big\{P^n_{i-1/2} - P^n_{i+1/2} - (A^n_{i-1/2} - A^n_{i+1/2})\sigma^n_i \\ & +3[(A^n_{i-1/2} + A^n_{i+1/2})\mu^{n+1}_i - (F^n_{i-1/2} + F^n_{i+1/2})m^n_i]\Big\}, \end{aligned} \tag{5.9}$$

with

$$P^n_{i+1/2} = \begin{cases} A^n_{i+1/2}\left(\sigma^n_i\left(\frac{A^n_{i+1/2}}{m^n_i}\right)^2 - 3F^n_{i+1/2}\right) & \text{if } A^n_{i+1/2} \geq 0; \\ A^n_{i+1/2}\left(\sigma^n_{i+1}\left(\frac{A^n_{i+1/2}}{m^n_{i+1}}\right)^2 - 3F^n_{i+1/2}\right) & \text{if } A^n_{i+1/2} < 0. \end{cases} \tag{5.10}$$

Together, equations (5.2), (5.6), (5.7), (5.9), and (5.10) form the basis of tracer transport by advection in TM5. It is important to realize that this routine is used alike in the three dimensions of advection (X, Y, and Z).

3 The convection routine

After the calculation of advection in X, Y, and Z direction, TM5 continues with vertical mixing (V). The basis of this routine, to which we refer as the convection routine, is explained in this section.

Where advection includes the - mostly horizontal - transport of trace gasses driven by the mean flow of air (wind), convection transports parcels vertically, and is driven by the heating of surface. Warm air parcels (close to the surface) have a lower density than the cold surrounding parcels and start to rise. Furthermore, a warm parcel of air can contain more moisture than a cold one. Once a parcel rises it cools down, and

---

be a typo. Namely, only for $\sigma_i = \frac{1}{2}s_i m_i^2$, their update is in line with the original slopes scheme determined by Russell and Lerner (1981).

part of the moisture condenses. In this way, clouds may form, which in turn enhance the transport of air as will be explained later on.

Vertical transport in the convection routine is done by redistributing tracer mass in the vertical column, and adjusting the slopes - as discussed previously in Section 2 - in three dimensions. The redistribution of the tracer mass depends on the flow of air masses throughout the vertical column, which is given in a $[l_{max} \times l_{max}]$ matrix C, also referred to as the 'convection matrix'. The entry $C(l,k)$ represents the fraction of air of layer k that is transported to layer l. The maximum layer to which convection is taken into account is l_{max}, and determines the size of the matrix. Realize that the air mass of each layer needs to be conserved, and that hence the sum of each column in C is equal to 1. Furthermore, the diagonal elements of C represent the fraction of air that remains in the same layer despite the convection. Since the concentrations of tracer are different between the layers, the mass of tracer in layer l after convection is calculated as the weighted average of the tracer masses in the upper and lower layers:

$$\mu_l^{n+1} = \sum_{k=1}^{l_{max}} C(l,k) \cdot \mu_k^n. \tag{5.11}$$

As an example we discuss a vertical column of three layers (see Figure 5.3). The tracer mass before convection is 10.0, 4.0, and 1.0 (arbitrary units) in layer 1, 2, and 3, respectively. By convection, layer 1 looses 40% of its air mass to layer 2, and 20% to layer 3. Layer 2 transports 20% of its mass to layer 3, and 10% back to layer 1. Lastly, 10% of layer 3 is transported downwards to layer 2, such that the convection matrix is as follows:

$$C = \begin{bmatrix} 0.4 & 0.1 & 0.0 \\ 0.4 & 0.7 & 0.1 \\ 0.2 & 0.2 & 0.9 \end{bmatrix} \tag{5.12}$$

Following (5.11), the distribution of tracer mass after convection is calculated by:

$$\begin{aligned} \mu_1^{new} &= 0.4 \cdot 10.0 + 0.1 \cdot 4.0 + 0.0 \cdot 1.0 = 4.4; \\ \mu_2^{new} &= 0.4 \cdot 10.0 + 0.7 \cdot 4.0 + 0.1 \cdot 1.0 = 6.9; \\ \mu_3^{new} &= 0.2 \cdot 10.0 + 0.2 \cdot 4.0 + 0.9 \cdot 1.0 = 3.8. \end{aligned} \tag{5.13}$$

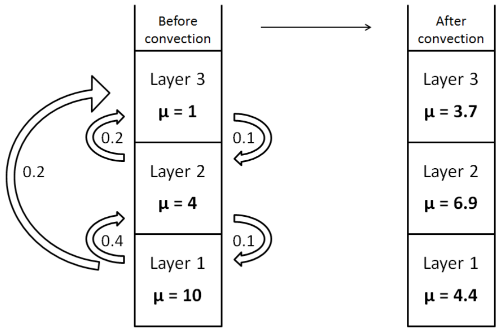

Figure 5.3: Example of vertical transport by the convection routine for a three-layer column. The tracer mass in each layer is given by μ, the air masses interchanging between the layers are stated next to the arrows and are expressed as the fraction of the total air mass of the originating layer.

After redistributing the tracer mass, slopes are updated in the convection routine as well (actually, $\sigma = \frac{1}{2}sm^2$ is updated). The horizontal slopes (σ_x, σ_y) are adjusted differently than the vertical ones (σ_z). For the first, the same procedure as with the tracer mass update is applied. Hence, the horizontal slopes are calculated as a weighted average of the horizontal slopes in the upper and lower layers:

$$\sigma_{\mathbf{x},l}^{n+1} = \sum_{k=1}^{l_{max}} C(l,k) \cdot \sigma_{\mathbf{x},k}^{n}. \tag{5.14}$$

Here, $\sigma_{\mathbf{x},l}$ is the horizontal slope ($\mathbf{x} = [x, y]$) in layer l. Matrix C is as before.

In convective areas, transport in the vertical is more efficient than in the horizontal. Hence, the vertical slopes are decreased slightly stronger than the horizontal ones:

$$\sigma_{z,l}^{n+1} = C(l,l) \cdot \sigma_{z,l}^{n}, \tag{5.15}$$

with $\sigma_{z,l}$ the vertical slope, and C as before. Instead of the weighted average of all layers, only the air mass that remaining in layer l itself determines the slope's update.

Overall, equations (5.11), (5.14), and (5.15) are the basis of the convection routine. How we adjusted and tested this routine to enhance transport in TM5 is explained in the next Chapter.

Chapter 6

Global SF_6 concentrations, problems and approach

Chapter 4 presents the conclusion that the optimization of a certain parameter in a transport model is done best for that parameter alone. Hence, either fluxes, or diffusion/transport should be optimized in our further optimizations, and not both at the same time. A tracer that can meet this requirement, since its emissions (fluxes) are quite well known, is the anthropogenic compound sulfur hexafluoride (SF_6). Section 1 discusses other, and beneficial, properties of SF_6 as well, and we identify this tracer suitable for our CTDAS optimizations. With a first SF_6 simulation in Section 2, we illustrate that interhemispheric transport in TM5 is too slow. Hereafter, Section 3 presents two methods to tackle the problem. Both enhance horizontal transport, and decrease the simulated concentration gradient that exist between the hemispheres. However, the first method tunes numerical diffusion that occurs due to the numerical scheme, whereas the second method aims to improve the actual physical process to explain enhanced horizontal transport.

1 The tracer SF_6

The trace gas SF_6 is a chemical compound that is released from high voltage electrical transformers. Emissions are purely anthropogenic, and hence quite well known. Besides, SF_6 has a long atmospheric lifetime ($\sim$ 3000 years) (Ravishankara et al., 1993), a sufficient number of observations, and does not interact with biological processes (Denning et al., 1999). Due to the last, SF_6 has only sources, and no sinks. Other favorable properties of SF_6 are its emissions that do not have seasonal variations, and a nearly constant increase of global atmospheric concentrations. The rate of this increase has an average of 0.20 $\text{ppt}\cdot\text{yr}^{-1}$ over the past decade (Peters et al., 2004). Considering all these properties, SF_6 is a suitable tracer to optimize transport properties in TM5 with. Some constraints on global SF_6 concentrations - that ideally are met by model simulations - are determined from observations by Gloor et al. (2007):

- The difference in concentrations between the Northern (NH) and Southern Hemispheres (SH), from here on referred to as the 'north-south gradient', is large at the surface. The gradient is steepest in the band between 25°N and 10°S. Between 30°N and 50°N, the latitudes where most SF_6 is emitted, large concentration differences occur over short distances. At other latitudes, SF_6 concentrations are distributed nearly uniform with latitude.

- The steep north-south gradient at the surface is much reduced in the upper troposphere. On shorter time scales, only part of the emissions - that mostly occur near the surface in the NH - reaches the upper layers of the atmosphere, and hence the difference with the SH is smaller at higher altitudes.
- Keeping in mind previous constraints, it is not surprising that the vertical profiles of SF_6 differ between the Northern and Southern Hemisphere. Emissions occur mostly in northern latitude regions, and cause high concentrations near the surface. Since the concentration of SF_6 in those regions is decreasing with altitude, a negative vertical gradient is observed. In the Southern Hemisphere, however, vertical profiles are opposite. Almost no emissions near the surface occur, ànd most of the SF_6 is transported to the south via the upper troposphere, such that positive vertical gradients are observed.
- Surface observations of SF_6 are sensitive to large scale atmospheric (seasonal) phenomena. For instance, vertical transport in the continental boundary layer is enhanced during summer due to more heating of the surface and hence stronger convection. Strong convection transports significant amounts of SF_6 to high altitudes, and surface observations have lower values than in winter. Another example is the seasonal undulation of the Intertropical Convergence Zone (ITCZ). The ITCZ is indicated as the region where the trade winds from both hemispheres come together and cause the strong updraft movements of the Hadley cell. In this way, air of the Northern Hemisphere is separated from air of the Southern Hemisphere. Seasonal movement of the ITCZ can bring 'Northern Hemisphere air', that is rich in SF_6, below the equator into the SH and vise versa.

In line with the constraints on atmospheric SF_6 as mentioned above, Peters et al. (2004) explain the mechanism by which SF_6 is transported from the Northern to the Southern Hemisphere. Namely, its transport over the equator mainly takes place in the free troposphere, where air from the northern Hadley cell ‘leaks’ into the southern Hadley cell. Even though this is a small amount for the NH (less than $\sim 5\%$ of the SF_6 transported into the tropics), it is the main input of SF_6 for the SH ($\sim 95\%$) (Peters et al., 2004). Although this mechanism is well understood, north-south transport of trace gasses is one of the main obstacles in transport models' simulations. Their performance, and that of TM5 in particular, is discussed in the next section.

2 Overestimation of the north-south gradient by TM5

Accurately simulating observed north-south transport of tracers is a challenge to most transport models. For instance, TM5 performs well in capturing temporal variability of SF_6 on all timescales, shows no large biases in its vertical profiles, but overestimates the interhemispheric gradient by 19% (Peters et al., 2004). This finding from literature is easily verified from the SF_6 simulations that we present in Figure 6.1. Plotted are SF_6 concentrations, modeled and observed, averaged over the year 2009 as a function of the sampled latitudes. Model values are only sampled at (marine) ‘background stations’, that measure the average background concentration of SF_6 rather than local variabilities - for instance caused by (land) emissions. We initialize our simulation with a concentration field of SF_6 in 2006, and consider one year as spin-up time for the model. In the subsequent years, the modeled gradient between northern and southern latitudes significantly overestimates the gradient of observations. The gradient in 2009 is provided in the figure. Note that SF_6 values are plotted relative to South Pole observations, such that the gradients of different years can be easily compared.

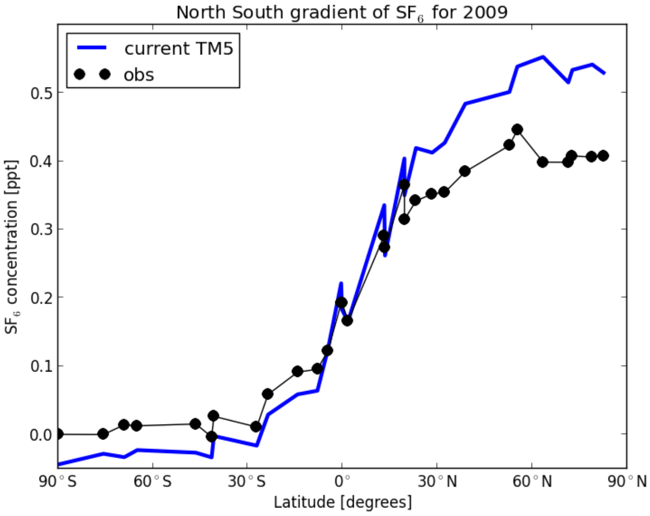

Figure 6.1: North south gradient of SF_6 averaged over 2009. Run time of the experiment is 2006 − 2009. The dots are observations at the selected stations (these are indicated with (B) in Appendix B), the blue line shows modeled values produced by TM5 as it is currently used. The average observed SF_6 concentration at the South Pole (SPO) in 2009 is subtracted from both observations and model samples.

In literature, different solutions to improve north-south transport of trace gasses are suggested. In their paper, Denning et al. (1999) state that - in line with their simulated vertical SF_6 profiles, and the differences between estimated gradients over land and sea - vertical trapping of trace gasses might be more controlling the north-south gradient than meridional transport itself. This conclusion is strengthened by the work of Stephens et al. (2007), that demonstrates a significant relation between estimated CO_2 fluxes and vertical transport in transport models. However, their analysis shows as well that TM3, which is the predecessor of TM5, is among the top three transport models concerning the simulation of annual mean vertical profiles of CO_2. The difficulty to achieve much improvement in TM5's vertical transport properties was already demonstrated by Peters et al. (2004). In this study, the northern Hadley cell's ‘leakage[1]’ is made more efficient by doubling the strength of convection in the transport model. By doing so, vertical transport is enhanced and more SF_6 might be transported from the NH to the SH. However, the overestimation of the north-south gradient (originally $\sim 19\%$) decreased with only two percent.

---

[1] This is explained in Section 1.

At the end of their paper, Stephens et al. (2007) state that besides vertical transport, horizontal transport (aloft) should be investigated as well. An early research - investigating (horizontal) transport of CFCs by transport models - suggests that sub grid diffusion should be introduced to improve simulation of the observed interhemispheric gradient of tracers, while its impact on the dynamics of the global circulation model is small (Prather et al., 1987). The parameterized diffusion should represent horizontal transport - occurring on sub grid scale - associated with deep convection in the vertical. Namely, horizontal transport of trace gasses in areas with deep organized convection can extent up to a few hundred kilometers (Zipser, 1969).

We use the approach of Prather et al. (1987) as a lead in this research: enhance horizontal transport, preferably in areas with strong convection, to improve north-south transport of trace gasses in TM5.

3 Methods for enhanced horizontal transport

We enhance horizontal transport in TM5 in two different ways. Section 3.1 explains how we adjust the horizontal slope's update in the convection routine, and presents the improved north-south gradient of SF_6. However, a precise match with observations is not reached still, and we address further enhancement of transport with the suggestion of Prather et al. (1987). In Section 3.2 we introduce explicitely parameterized sub grid diffusion, and link it to strong convective updrafts, analogous to their work. Actual optimization of the transport parameter will be discussed later in Chapter 7.

3.1 Adjustment of the slopes

A main advantage of the slopes scheme[2] in TM5 is that concentration gradients within grid boxes are accounted for, such that the model is more spatially detailed without actually increasing resolution. Furthermore, these spatial gradients can be maintained in time in contrast to the diffuse upwind scheme. By tuning the (horizontal) slopes to enhance horizontal tracer transport, one actually tunes TM5 between a strong conservative slopes numerical scheme and a less conservative upwind scheme. This should be done with caution. We find an inconsistency between the horizontal and vertical slopes update, and hence consider an adjustment suitable. Recall that the time step update of horizontal slopes is a weighted average of the slopes in upper and lower layers (see equation (5.14)). For vertical slopes, however, only the fraction of air and the current slope determine the slope's update (see equation (5.15)). This update is less conservative, and thus allows more transport.

We consider it arguable that due to convection slopes in all directions are mixed equally, and not differently, for the horizontal and vertical direction. To align the updates at each time step, and to enhance horizontal transport, we propose to use the less conservative slope update of the vertical in horizontal directions as well. Hence, we implement:

$$\sigma_{\mathbf{x},l}^{n+1} = C(l,l) \cdot \sigma_{\mathbf{x},l}^{n}, \tag{6.1}$$

with $\sigma_{\mathbf{x},l}$ the slopes in horizontal ($\mathbf{x} = [x, y]$) direction, and C the convection matrix as before.

---

[2] Recall from Chapter 5, Sections 2 and 3.

Even though implementation of the above might seem a rather basic adjustment, the impact on north-south transport of SF$_6$ is significant. In Figure 6.2 we show SF$_6$ concentrations as a function of latitude, with the setup as before. From the plot, it is clear that the observations (black dots) are better represented with enhanced horizontal transport (red line) than with the old slopes scheme (blue line). This conclusion is strengthened by a decrease in the RMSD between model and observations from 0.070 to 0.047.

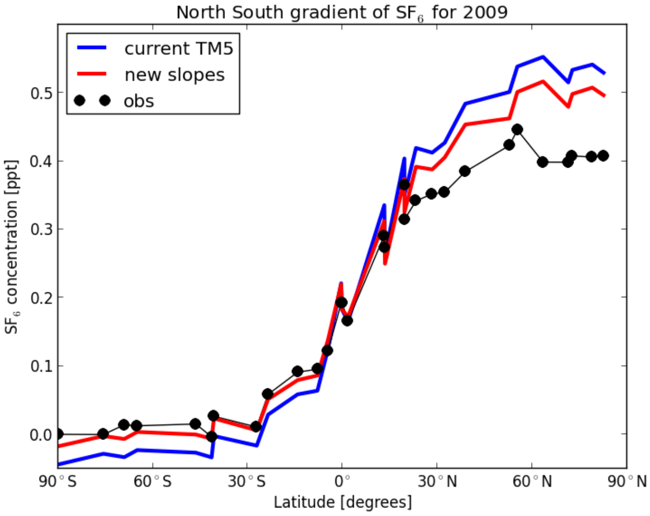

Figure 6.2: North south gradient of SF$_6$ averaged over 2009. Runtime of the experiment is 2006 – 2009. The black dots are observations at the selected stations (these are indicated with (B) in Appendix B). The blue line shows TM5 as it is currently used, whereas the red line contains TM5 with the adjusted horizontal slope update of equation (6.1). The average observed SF$_6$ concentration at the South Pole (SPO) in 2009 is subtracted from both observations and model samples.

From here on, we equip TM5 with the slopes update of (6.1), and refer to this as the 'basecase'. Now, we examine if more improvement of transport is possible by further tuning of the slopes. We implement the reduction by scaling the horizontal slopes update with a factor α that can take values between 0 and 1:

$$\sigma_{\mathbf{x},l}^{n+1} = \alpha \cdot C(l,l) \cdot \sigma_{\mathbf{x},l}^{n}. \tag{6.2}$$

Here, $\sigma_{\mathbf{x},l}$ represent the slopes in horizontal ($\mathbf{x} = [x,y]$) direction, C the convection matrix as before, and α the reduction factor. As explained in Section 2, we aim to link horizontal transport to deep convective areas in order to explain the process. We therefore set the condition that only if:

$$C(l,l) < 0.95, \tag{6.3}$$

is satisfied (an indication for convective movement, since more than 5% of the air in the box originates from upper and lower layers), the slopes reduction of (6.2) is activated, otherwise the slopes are updated according to (6.1). However, TM5 appears to be rather insensitive to (a change in) α in regions where $C(l,l)$ already has a value smaller than 0.95. Only in regions where $C(l, l) = 1$ (no convection occurs), the reduction with $\alpha < 1$ is effective. It is precisely in those regions that we do not wish to enhance horizontal transport, and we consider the method unsuitable for our purpose.

Besides, further reduction of the slopes is doubtful, since this would negate the function of the slopes numerical scheme with its ability to capture gradients within grid boxes (especially important in emission regions, where strong spatial gradients occur). We consider returning to the upwind scheme as undesirable, and hence reject the enhancement of horizontal transport via a slopes reduction factor.

3.2 Explicitly parameterized diffusion

Since we consider the previous method unsuitable, we implement another approach in the convection routine, that is largely analogous to the one of Prather et al. (1987). The theory behind the parameterization starts with large updraft movements that occur in strong convective areas, and often cause the formation of clouds. The updrafts are balanced by downdraft movements to maintain a mass balance, but also at the edge of the clouds, turbulent transport of air takes place. When air is mixed into the cloud, this is called 'entrainment'. On the contrary, 'detrainment' is associated with air that moves from the interior of the cloud to the surrounding air. An illustration of this process is provided in Figure 6.3.

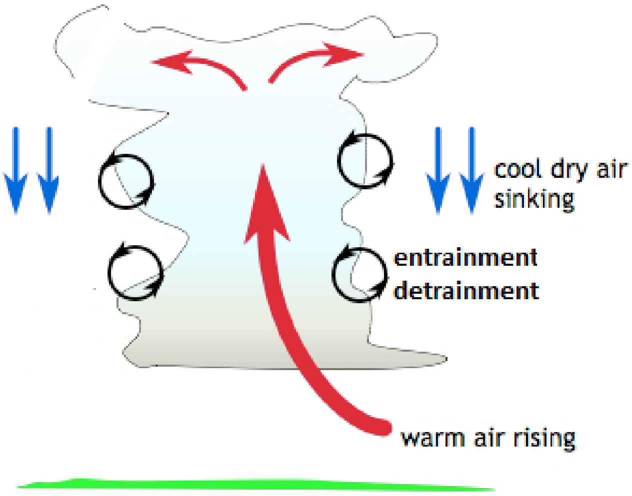

Figure 6.3: Updraft and downdraft movements in a deep convective cell. Entrainment and detrainment of air occur at the cloud edge. The figure is adjusted from the website of the Center for Multiscale Modeling of Atmospheric Processes (2013).

In this research we aim to enhance horizontal transport of tracer in regions with strong convective motions as in Figure 6.3. We assume that the entrainment and detrainment fluxes in a grid box are a good proxy for the strength of such motions, and we use them to determine a diffusion coefficient K - not to be confused with the Kalman gain matrix as explained in Chapter 2. Later on, this coefficient is used to parameterize horizontal transport as a diffuse process. We obtain $K_{i,j,l}$ by summing the entrainment and detrainment fluxes in layer l in grid box i, j, scaling it with the surface area of the box, and the total air mass. More specifically, entrainment and detrainment at the cloud base determine the diffusion coefficient under the cloud. In the cloud, $K_{i,j,l}$ is calculated for each layer separately - with the entrainment/detrainment fluxes of the cloud layers:

$$K_{i,j,l} = \begin{cases} \frac{A_{i,j}}{m_{i,j,c_{base}}} \cdot (E_{i,j,c_{base}} + D_{i,j,c_{base}}) & \text{for} \quad l = 1, \ldots, c_{base}; \\ \frac{A_{i,j}}{m_{i,j,l}} \cdot (E_{i,j,l} + D_{i,j,l}) & \text{for} \quad l = c_{base} + 1, \ldots, c_{top}. \end{cases} \tag{6.4}$$

Here, $A_{i,j}$ is the surface area of the grid box in m^2, $m_{i,j,l}$ its total mass in kg, and $E_{i,j,l}$ and $D_{i,j,l}$ represent the total entrainment and detrainment fluxes in $kg \cdot s^{-1}$, respectively. This results in a diffusion coefficient in $m^2 \cdot s^{-1}$, which is in accordance with the units of the - differently - determined coefficient by Prather et al. (1987). Typical values of K vary from $\sim 3.5e7\frac{m^2}{s}$ in the tropics to $\sim 1.0e7\frac{m^2}{s}$ in the mid-latitudes ($\sim 1.3e7\frac{m^2}{s}$ in summer, and $\sim 0.7e7\frac{m^2}{s}$ in winter), and to 0-$5e4\frac{m^2}{s}$ in the polar regions. Values are highest near the surface and decrease with altitude.

To ensure that horizontal transport is only affected in strong convective areas, calculations of $K_{i,j,l}$ as in (6.4) are only done for vertical columns that contain deep convective clouds. We define:

$$c_{top} - c_{base} > 500 \text{ hPa} \tag{6.5}$$

as the lower bound for cloud depths to activate enhanced transport in the convection routine. Here, c_{base} and c_{top} are the height of the cloud base and cloud top in hPa, respectively. In columns where (6.5) does not hold - and where we assume that no deep convection occurs - we set $K_{i,j,l} = 0$ for all l in the column.

A short remark: the diffusion coefficient is equal in both horizontal directions, such that:

$$K_{x,i,j,l} = K_{y,i,j,l} = K_{i,j,l}. \tag{6.6}$$

Once the diffusion coefficient is determined, it is used as a measure for horizontal transport of trace gasses. The larger K, the more tracer is transported between adjacent grid boxes. The actual mass fluxes of tracer are obtained similarly to the fluxes by Prather et al. (1987). Namely, the average diffusion coefficient of two adjacent grid boxes is multiplied with their average mass, and with the difference in trace mass fraction between the boxes. Lastly, this product is scaled with the time step and a length scale. In the west-east horizontal direction (x) we have:

$$F_{x,i+1/2} = \frac{\Delta t}{\Delta x^2} \cdot \frac{K_i + K_{i+1}}{2} \cdot \frac{m_i + m_{i+1}}{2} \cdot \left(\frac{\mu_i}{m_i} - \frac{\mu_{i+1}}{m_{i+1}} \right), \tag{6.7}$$

with Δt the time step (in s), and Δx the length of the grid box (in m). Other symbols are as defined previously. Calculation in the south-north horizontal direction (y) is done similarly:

$$F_{y,j-1/2} = \frac{\Delta t}{\Delta y^2} \cdot \frac{K_j + K_{j+1}}{2} \cdot \frac{m_j + m_{j+1}}{2} \cdot \left(\frac{\mu_j}{m_j} - \frac{\mu_{j+1}}{m_{j+1}} \right). \tag{6.8}$$

Combined, (6.7) and (6.8) determine the in- and outgoing horizontal fluxes of tracer for a grid box in column i, j as illustrated in Figure 6.4. Hence, the update for the tracer mass at each time step is:

$$\mu_{i,j}^{n+1} = \mu_{i,j}^{n} + F_{x,i-1/2}^{n} - F_{x,i+1/2}^{n} + F_{y,j-1/2}^{n} - F_{y,j+1/2}^{n}. \tag{6.9}$$

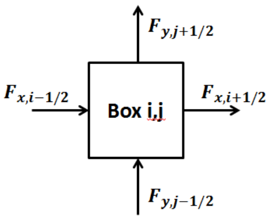

Figure 6.4: Fluxes (F) of tracer in the horizontal domain for grid box i, j.

To be consistent with the mass transport, the slopes are updated according to the work of Prather et al. (1987). Namely, they are decreased by a factor that corresponds with the strength of the diffusion coefficient:

$$\sigma_{x,i}^{n+1} = \sigma_{x,i}^{n} \cdot \max\left\{0, 1 - 2 \cdot K \cdot \frac{\Delta t}{\Delta x^2}\right\}, \tag{6.10}$$

for the west-east direction, and:

$$\sigma_{y,j}^{n+1} = \sigma_{y,j}^{n} \cdot \max\left\{0, 1 - 2 \cdot K \cdot \frac{\Delta t}{\Delta y^2}\right\}, \tag{6.11}$$

for south-north direction. It is important to realize that (6.9), (6.10), and (6.11) are calculated for each vertical layer l separately.

The diffusion coefficient K is a measure for the strength of convection, and hence suitable to indicate the strength of the enhanced transport. However, to obtain realistic values for the mass fluxes (equations (6.7) and (6.8)) and slope updates (equations (6.10) and (6.11)), it needs to be scaled by a factor. Herefore, we introduce the parameter δ in equations (6.7), (6.8), (6.10), and (6.11). They become:

$$F_{x,i+1/2} = \frac{\Delta t}{\Delta x^2} \cdot \delta \cdot \frac{K_i + K_{i+1}}{2} \cdot \frac{m_i + m_{i+1}}{2} \cdot \left(\frac{\mu_i}{m_i} - \frac{\mu_{i+1}}{m_{i+1}}\right), \tag{6.12}$$

$$F_{y,j-1/2} = \frac{\Delta t}{\Delta y^2} \cdot \delta \cdot \frac{K_j + K_{j+1}}{2} \cdot \frac{m_j + m_{j+1}}{2} \cdot \left(\frac{\mu_j}{m_j} - \frac{\mu_{j+1}}{m_{j+1}}\right), \tag{6.13}$$

$$\sigma_{x,i}^{n+1} = \sigma_{x,i}^{n} \cdot \max\left\{0, 1 - 2 \cdot \delta \cdot K \cdot \frac{\Delta t}{\Delta x^2}\right\}, \tag{6.14}$$

and:

$$\sigma_{y,j}^{n+1} = \sigma_{y,j}^{n} \cdot \max\left\{0, 1 - 2 \cdot \delta \cdot K \cdot \frac{\Delta t}{\Delta y^2}\right\}, \tag{6.15}$$

respectively. With CTDAS, we aim to optimize the scaling factor, or ‘transport parameter’, δ, in order to improve horizontal transport in TM5.

To verify that the scheme is indeed suitable to enhance north-south transport of SF$_6$, we test different diffusion scaling parameters. Figure 6.5 provides the resulting north-south gradients for some relevant δ.

Obviously, the dashed magenta line in the figure illustrates that disregarding a scaling factor for K ($\delta = 1.0$) leads to a model bias in horizontal transport. Values around $\delta = 0.1$, and $\delta = 0.2$ are more appropriate, and show a better match with

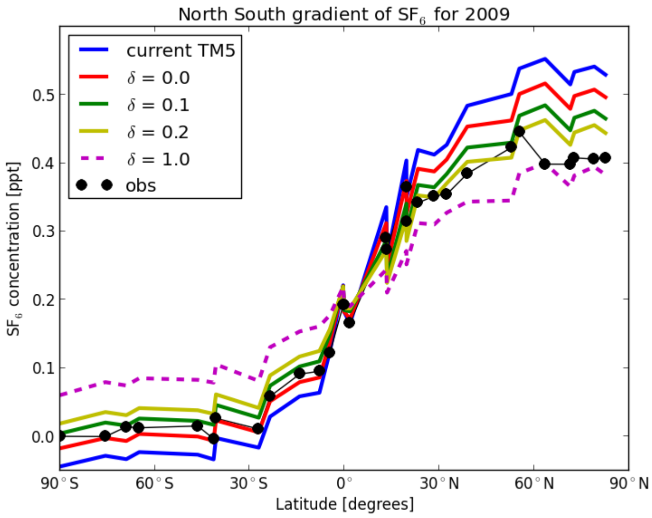

Figure 6.5: North south gradient of SF$_6$ averaged over 2009. Run time of the experiment is 2006 − 2009. The dots are observations at the selected stations (these are indicated with (B) in Appendix B), the colored lines show modeled values for different diffusion scaling parameters δ. Note that $\delta = 0.0$ is equal to our previously defined basescase. The average observed SF$_6$ concentration at the South Pole (SPO) in 2009 is subtracted from both observations and model samples.

observations. RMSD values of these runs are comparable (0.033 and 0.031), but parameterizing transport with $\delta = 0.2$ overestimates observations at the South Pole, where these were underestimated before. Hence, we consider $\delta = 0.1$ as the most suitable prior for further optimizations with CTDAS.

Overall, TM5, with the slopes update of (6.1) included in the convection routine, has stronger horizontal transport than before, and is considered as our basecase. Figure 6.5 shows that interhemispheric transport can be further enhanced by parameterizing horizontal diffusion. In this scheme, a transport parameter scales the diffusion to obtain the actual strength of enhanced transport. We propose to optimize this transport parameter with CTDAS in order to obtain improved interhemispheric mixing in TM5.

Chapter 7

Optimization of transport: setup and results

Section 1 discusses the optimization of one global transport parameter to improve interhemispheric transport in TM5. Section 2 aims to obtain knowledge on the spatial variation in horizontal transport, by dividing the world into five regions, and hence optimizing five transport parameters.

1 One global transport parameter

Section 1.1 presents the optimization setup of CTDAS for one global transport parameter. Hereafter, Section 1.2 evaluates the results, and Section 1.3 presents interim conclusions on a suitable value for the transport parameter.

1.1 Setup

Recall from Chapter 2 that observations, model-data-mismatch - representing the covariance of the observations -, a priori state vector estimates, and (the number of) ensemble members - representing the covariance of the a priori estimates - are important factors for the CTDAS setup. Also, the cycle length, determining the interval over which the state vector is optimized, should be taken into account. We identify the following setup for one global parameter optimizations with CTDAS:

- Observations;

We obtain SF_6 observations from the National Oceanic and Atmospheric Administration (NOAA) surface flask network. Hereof, we only select so-called ‘background stations’. These stations mostly are located in the marine boundary layer (over the oceans), far away from the sources on land. Hence, they measure large scale - background - concentrations rather than local variations. Appendix B provides details on the selected background stations, as well as on the total network.

We validate our model results with NOAA (surface/aircraft) flask data, but more importantly with independent data of the HIAPER Pole-to-Pole Observations (HIPPO) project as well (Wofsy et al., 2012). The scientist in this project collected measurements of many greenhouse gases, including SF_6, at all latitudes and many altitudes (from 300 up to 14.000 meter) during several pole-to-pole flights in the years 2009-2011.

- Model-data-mismatch;

Uncertainty of observations is considered in the data assimilation system, and represented by the covariance matrix R. The diagonal elements of R represent the model-data-mismatch of the different stations, and indicate an uncertainty range (σ) around observations which modeled values should account for. We determine this uncertainty for each station separately by fitting its SF_6 time series (2006-2011) with a second order polynomial, and subtracting the trend. The standard deviation of the residuals is taken as the model-data-mismatch at that specific station. Since only background stations are selected, observations are rather accurate, and the uncertainty values range between 0.02 and 0.12 ppt.

- A priori estimate;

One global transport parameter is assimilated with CTDAS, such that the state vector has length one as well. Section 3.2 of Chapter 6 identifies 0.1 as an appropriate value for the transport parameter δ (in the EnKF stated as as $\mathbf{x}$), and we take this as the a priori estimate of the state vector: $\mathbf{x_0} = 0.1$.

Usually, the optimized state vector is propagated as the a priori estimate of the next cycle. Besides, we test another propagation of the state vector, that is useful to avoid instability of the transport parameters. In these simulations, we set the a priori estimate to its first prior value every cycle, and we refer to them as ‘fixed prior’ simulations.

- Ensemble members;

Uncertainty of the a priori estimate is accounted for in data assimilation as well, this time in the covariance matrix P. Special about CTDAS is that an ensemble of state vectors (ensemble members) represent P, as is stated with equations (2.11), (2.12), and (2.13) previously. Actually, the a priori state vector is considered as the mean of the ensemble, and the different members represent the (co-)variance around it. They are taken from a normal distribution around 0, and added to the prior.

To avoid negative diffusion in TM5, we do not allow negative transport parameters ($\mathbf{x_0}'$), and hence use a semi-exponential probability destiny function (PDF) for the ensemble members (Bergamaschi et al., 2009). A dummy value a is taken from a normal distribution with $\mu_a = 0.0$, and $\sigma_a = 0.5$. Herewith, the (positive) ensemble members are calculated:

$$\mathbf{x_0}' = \begin{cases} \mathbf{x_0} \cdot \exp^a & \text{if} \quad a < 0; \\ \mathbf{x_0} \cdot (1 + a) & \text{if} \quad a \geq 0. \end{cases} \tag{7.1}$$

An ensemble member is indicated with $\mathbf{x_0}'$, the a priori state vector with $\mathbf{x_0}$. Note that by this modification the actual covariance of the ensemble members is approximately:

$$\sigma_{\mathbf{x_0}'} \approx \mathbf{x_0} \cdot \sigma_a = 0.1 \cdot 0.5 = 0.05. \tag{7.2}$$

Figure 7.1 depicts the PDF of the semi-exponential distributed ensemble members, where members created with $a < 0$ are distributed between zero and the mean (0.1). Since this is a smaller domain than originally (between $-\infty$ and the mean), a peak in the PDF next to the mean occurs.

Figure 7.1: Probability density function (PDF) of the ensemble members (red line), values below zero do not occur due to the semi-exponential distribution. Note that the PDF is comparable to a distribution with $\mu = 0.1$, and $\sigma = 0.05$ (blue line).

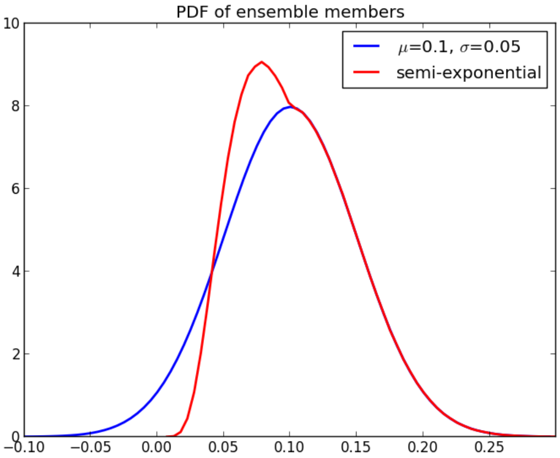

Now, values of δ range between 0.0 and 0.25 (99.85% of values is smaller than $\mathbf{x_0} + 2\sigma_{\mathbf{x_0}'}$) for all members. This covariance range is suitable for the optimization of δ, since we previously concluded that $\delta = 0.0$ induced too weak, and $\delta = 0.25$ too strong horizontal transport in TM5. The optimal value we propose to find with CTDAS must lie in between.

Since we optimize one global transport parameter, and abundant observations are available, 10 ensemble members are used to represent the a priori state vector's covariance.

- Cycle length and lag;

The cycle length in CTDAS determines the interval over which the state vector is optimized. Additionally, the system can be used as a 'filter', or a 'smoother'. With the first, the relation between model and observations is exactly evaluated within the cycle length period (lag = 1). With CTDAS as a smoother (lag $= 2, 3, 4, \ldots$), the state vector is still updated every cycle, but the effect on the concentration field is considered for a longer time span. For instance, an optimization with a cycle length of 90 days, and lag = 2, calculates an updated state vector every season, while taking into account its effect on the concentrations over half a year. For a detailed explanation of the smoother in CTDAS we refer to the paper by Peters et al. (2005). However, CTDAS as a smoother has only a minor role in this research, since its results do not differ significantly from the filter optimizations. Hence we optimize for both yearly transport parameters (cycle length is 365 days), and seasonally parameters (cycle of 90 days).

- Emissions:

The SF_6 emissions that are fed to the model are of main importance for our optimizations. Namely, we do not want CTDAS to correct TM5's transport for biases in emissions. We use SF_6 emissions from the EDGAR (2009) for the years 2006-2007, and extrapolate these to obtain emissions for the years 2008-2009. Herefore, we scale 2007 emissions with the average observed annual growth rate (which is rather constant for SF_6) at two background stations, Mauna Loa (MLO) and South Pole (SPO), divided by the rate of 2007. In this way, we assure that our emissions match the annual global trend in SF_6, and that the total concentration in the atmosphere is correct. We verify that indeed no systematic biases in our emissions exist by analyzing modeled and observed SF_6 time series at different stations. In all cases, the observed trend in concentrations is captured well. At some stations a (small) offset occurs though, but this can be related to incorrect transport in TM5.

- Resolution;

All optimizations are performed on a 6° × 4° grid. Hence, the whole globe consists of 60 grid boxes in the zonal and 45 boxes in the meridional direction.

1.2 Results

Table 7.1 displays the results of one global transport parameter optimizations for different configurations. The simulations are initialized in 2006 with a concentration field that closely matches observations. Hence, one year of spin-up time is sufficient, and we use the optimized values of δ of the three consecutive years (2007-2009) for our analysis. Figure 7.2 displays the evolution in time of the transport parameter.

Table 7.1: Results of one global transport parameter optimizations. The cycle length is given in days; the column 'fixed prior' indicates whether or not the state vector is propagated in the optimization; CTDAS is used as a filter (lag = 1) in most cases, sometimes as a smoother (with lag = 2). The average and standard deviation of δ over the years 2007-2009 is provided under μ and σ, respectively.

				ERA-Interim		Operational Data	
Nr.	Cycle length	Fixed prior	Lag	μ_δ	σ_δ	μ_δ	σ_δ
1	365	No	1	0.15	0.03	0.10	0.01
2	365	Yes	1	0.14	0.02	0.12	0.02
3	90	No	1	0.08	0.04	-	-
4	90	Yes	1	0.09	0.03	0.08	0.06
5	90	No	2	0.08	0.03	0.06	0.02
6	90	Yes	2	0.09	0.02	0.08	0.02

Parameter values deviate from cycle to cycle, yet no large outliers are present. We average the values of δ over 2007-2009, and present them with their standard deviation in Table 7.1. Recall that for each simulation we obtain two values, as we consider two types of meteo data (ERA-Interim and Operational Data).

We check that our simulations are robust by assimilating with a double amount of ensemble members (20 instead of 10), such that the a priori covariance is better represented. Also, we perform a simulation with different (fixed) a-prior estimates. Both tests provide comparable results with the original simulations, confirming that the transport parameter is assimilated properly. Moreover, we find that using a lag does not change our optimizations, and we will not assess it further in this research. Fixing or propagating the prior also does not impact the optimized transport parameters significantly, provided that this prior is close enough to the optimal solution.

Figure 7.2: Yearly (top figure) and seasonally (bottom figures) optimization of one global transport parameter δ. The numeration of the simulations matches the configurations as stated in Table 7.1. Mean values of δ over the years 2007-2009 are given next to the plots.

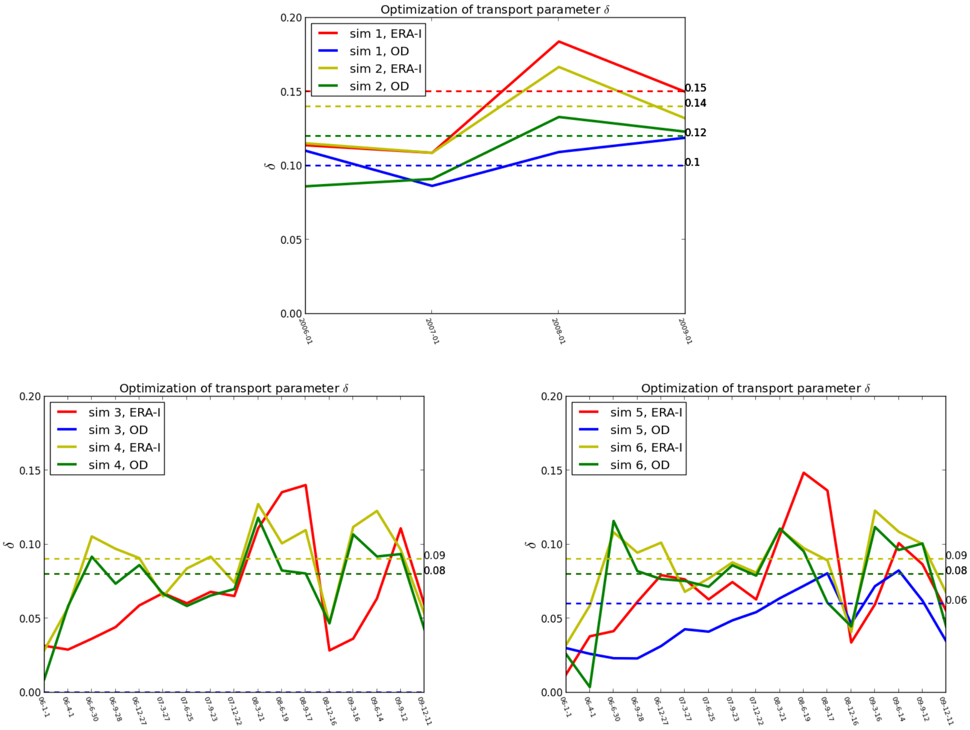

From Table 7.1, we find that δ is estimated largest for yearly optimized transport, and somewhat smaller for seasonally transport. We can explain this from a data-assimilation perspective, as well as from the perspective of atmospheric transport itself. To explain the first, we assume that the transport model's sampled deviations ($\mathcal{H}(\mathbf{x}')$) are sensitive for long cycle lengths, since the state vector deviations ($\mathbf{x}'$) are then propagated over a long time period. This might result in a sensitive, and possibly larger, Kalman gain matrix (K), such that rather rigorous state vector updates, and higher values, can occur.

Yet, we consider as best explanation the impact of the so-called 'rectifier effect'. This effect is known as the combination of covariances in both atmospheric transport and the (biospheric, in the case of CO_2) flux (Chan et al., 2008). For example, Chan et al. (2008) explain that variations in transport and CO_2 concentrations have a different timing, and that this causes a higher annual mean of CO_2 in northern high latitudes. Namely, meridional transport in winter is twice as strong as it is in summer, since the large temperature gradient between the tropics and the poles in winter drives strong horizontal transport of air by large-scale eddies. At the same time, CO_2 concentrations in the atmosphere are relatively high in winter, due to plant respiration, and relatively low in summer, due to photosynthetic uptake of the biosphere. Combining these temporal variances, low CO_2 concentrations are transported less, whereas high concentrations in winter are transported more efficiently, resulting in the high annual mean in the northern polar region (Chan et al., 2008).

Applying the concept of the rectifier effect on our SF_6 simulations, we state that, although atmospheric concentrations do not change throughout the year, the variance in transport patterns explains the difference between the relatively high and low values of δ for yearly and seasonally optimizations, respectively. At first, we argue that, in accordance with the work of Chan et al. (2008), meridional transport in winter is strong, such that (extra) transport in the form of parameterized diffusion is less needed than in summer. Moreover, strong convective updrafts occur less in winter, and our parameterization scheme, activated by deep convective clouds, is most effective in the summer season. Apparently, parameterizing enhanced transport in certain periods (mainly in summer, as displayed in Figure 7.2) is sufficient to improve the SF_6 concentration distribution in TM5, and can be achieved with a seasonally assimilated transport parameter. A yearly cycle length cannot capture these temporal variabilities and requires an overall higher δ.

Lastly, we find from Table 7.1, that results of the two meteorological data types are comparable for the different configurations. Transport parameters estimated with ERA-Interim, however, are slightly larger than the parameters estimated with Operational Data, indicating that optimizing transport cannot be done completely independent of the meteorological data input. We verify that the north-south gradient of SF_6 concentrations, as displayed in Figure 6.1 for ERA-I, is slightly better with OD meteo data. This suggests that horizontal transport is better represented in the OD meteorology, such that less 'extra' horizontal diffusion is required in TM5 than for ERA-I meteorology.

1.3 Interim conclusion on one transport parameter

Because the implementation of a (yearly/seasonally) varying parameter is impractical in TM5, we determine one parameter value from Table 7.1 is most suitable to enhance horizontal transport in TM5. We deem the yearly estimated transport less suitable than the other simulations, since it captures no seasonal variations, and requires stronger impacts to TM5 by the diffusion parameterization. Figure C.1 in Appendix C illustrates this with the average RMSD at all measurement stations over the year 2009, of simulations using $\delta = 0.15$, $\delta = 0.1$, and $\delta = 0.08$ (the two extreme values of ERA-I, and the prior). It is clear that $\delta = 0.15$ gives a better match with observations at northern latitudes (Alert (Canada), Azores (Portugal), Storhofdi (Iceland), Summit (Greenland), and Ny-Alesund (Norway and Sweden)) than $\delta = 0.08$. Yet, the effect on the Southern Hemisphere is opposite, and $\delta = 0.15$ overestimates most stations there.

Overall, we conclude that $\delta = 0.09$ improves concentrations in the NH, without overestimating concentrations in the SH, and we propose to use $\delta = 0.09$ in the parameterization scheme with one global transport parameter. We realize that the distinction between $\delta = 0.08$, $\delta = 0.09$, or the prior $\delta = 0.1$ cannot be made, since the standard deviation range on the optimized parameters captures all three solutions, and the global concentration distribution is comparable for these parameters. Hence, we may validate our results for $\delta = 0.1$ (instead of $\delta = 0.09$), as we will do in Chapter 8.

2 Five transport parameters

Besides seasonal variation in (one) transport (parameter), as evaluated in the previous section, spatial variation might be relevant as well. Section 2.1 presents the setup of simulations to capture this variation by using five, instead of one, transport parameters. Section 2.2 discusses the results, whereafter Section 2.3 presents some first conclusions.

2.1 Setup

To capture spatial variability in the parameterization of transport, we determine five regions by separating the globe at the latitude bands 60°N, 30°N, 30°S, and 60°S. The new state vector consists of five elements (δ_i, with $i = 1, \ldots, 5$), and each element represents the transport parameter in one of the regions. The data-assimilation system now contains four more degrees of freedom, and hence we increase the number of ensemble members representing the a priori covariance to 25.

Whereas the optimization of one transport parameter was rather constraint (because this one parameter was applied over the whole globe), the five transport parameters are updated separately, and mainly try to match observations within their reach (the specific region they are linked to). From first optimizations, it turns out that δ_2 increases after each optimization cycle. High transport parameters mean high diffusion coefficients, that might drain all SF_6 out of grid boxes. This causes negative concentrations in TM5, and a crash of the system is unavoidable. From previous simulations we learned that fixing the prior does not impact one optimized transport parameter, provided that the prior is close enough to the optimal solution. Since only δ_2 intended to increase after each cycle, we consider it suitable to apply a fixed prior of 0.1 to all parameters. This avoids the instability of δ_2, without influencing the outcome of the other parameters.

Lastly, CTDAS is used as a filter (lag = 1) in all simulations. The remaining factors of the setup are equal to our previous simulations.

2.2 Results

In Table 7.2, we present the results of regional transport parameter assimilations. Figure 7.3 displays the propagation in time of the parameters.

Table 7.2: Results of the optimizations of five transport parameters. The cycle length is given in days. The a priori estimates are fixed ($\mathbf{x_0} = [0.1, 0.1, 0.1, 0.1, 0.1]$), and CTDAS is used as a filter (lag = 1) in all cases. The average and standard deviation of δ over the years 2007-2009 is provided under μ and σ, respectively.

Nr.	Cycle length	Meteo	δ_1		δ_2		δ_3		δ_4		δ_5	
			μ	σ	μ	σ	μ	σ	μ	σ	μ	σ
7	365	ERA-I	0.15	0.02	0.37	0.04	0.10	0.03	0.13	0.06	0.13	0.02
		OD	0.09	0.02	0.38	0.08	0.07	0.01	0.19	0.06	0.13	0.01
8	90	ERA-I	0.10	0.01	0.18	0.04	0.07	0.03	0.10	0.02	0.10	0.01
		OD	0.11	0.02	0.16	0.02	0.06	0.03	0.10	0.02	0.10	0.02

Figure 7.3: Yearly (top figures) and seasonally (bottom figures) optimization of five transport parameters δ_i. The numeration of the simulations matches the configurations as stated in Table 7.2. Mean values of δ_i over the years 2007-2009 are given next to the plots.

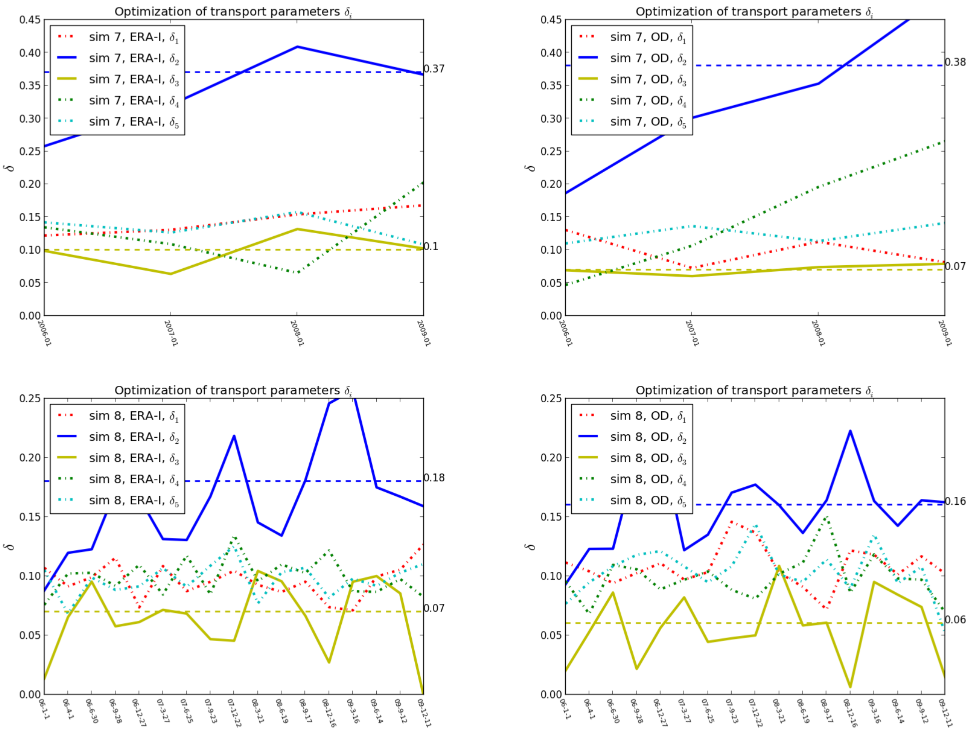

The most striking result are the high values for δ_2, the transport parameter in the northern mid-latitude region (between 30° and 60° N). Other parameters stay rather close to their prior value. However, results of parameters δ_1, δ_4, and δ_5 are misleading. Namely, their covariance after optimization (recall the matrix P_{opt} as in (2.7), not to be confused with the standard deviation provided in Table 7.2) did not decrease compared to the a priori covariance (recall matrix P_0 or P as in (2.12). This suggests that these parameters did not gain information from the assimilation, and are updated randomly.

In order to explain the above, we evaluate the representation of convective precipitation (on $1 \times 1°$ grid resolution), and the resulting cloud depth (on $6 \times 4°$ grid resolution) in the ERA-I meteorological data. Appendix D displays both on a global map for a winter and a summer month (in 2008). From the maps we identify that, especially in Northern Hemisphere winter, (almost) no deep convection occurs in regions 1, 4, and 5. In these regions, the diffusion parameterization scheme cannot be triggered, and the parameters cannot be optimized with CTDAS. Hence, only transport in the tropics and northern mid-latitude regions, represented by δ_2 and δ_3 respectively, can be assessed further.

In accordance with our previous results, simulations with cycles of 365 days show larger transport parameters than simulations with cycles of 90 days. We use the same reasoning as in Section 1.2.

Interestingly, the seasonally optimized transport parameters show temporal variations, whereby δ_2 and δ_3 seem to be correlated. Indeed, correlation coefficients between δ_2 and δ_3 range from ~ 0, mostly obtained in winter, to -0.4, mostly obtained in summer. Abundant deep convection in NH summer assures that horizontal transport is most efficiently enhanced in the tropics (peak in δ_3) in this period. Linked to this, less enhancement in northern mid-latitudes is required (dip in δ_2). In NH winter, however, enhancement in the tropic is less required/efficient, such that δ_3 drops to lower values. At the same time, most deep convection disappears in northern mid-latitudes, while enhanced transport is needed still. With the few convective clouds triggering the parameterization scheme, CTDAS tries to enhance transport in the region, such that δ_2 is estimated as high as possible (it is constrained though by the fixed prior at 0.1).

2.3 Interim conclusion on five transport parameters

To determine whether spatial variation in horizontal transport parameterization can improve the global distribution of SF_6 concentrations, we again observe the RMSD at all measurement stations for the simulations, and compare them to the a priori estimate. Figure C.2 in Appendix C shows that $\delta = [0.10, 0.18, 0.07, 0.10, 0.10]$ (simulation 9) does not significantly change the match with observations compared to the prior. Results of simulation 8 ($\delta = [0.15, 0.37, 0.10, 0.13, 0.13]$), however, are comparable to the prior at the SH, and slightly improve the match with observations at high latitude station in the NH.

Overall, parameters of simulation 8 capture seasonal variability in the transport parameter, but cannot compete with the strong enhanced transport in northern mid-latitudes of simulation 7 ($\delta_2 = 0.37$). We state that indeed spatial variation in parameterized diffusion can improve transport in TM5. Yet, the improvement we obtain with our optimized values is small, and more research on correlations, appropriate regions and/or parameter values is required.

Chapter 8

Validation

In Chapter 6 we tuned the difusivity of TM5's numerical scheme, and Figure 6.2 justifies that this enhances horizontal mixing effectively. Hereafter, in Chapter 7, we found $\delta = 0.09$ as a suitable value to parameterize horizontal transport on a $6^\circ \times 4^\circ$ grid. We identified that $\delta = 0.1$ is a proper solution within the uncertainty range, and use it in this chapter to validate our results. The spatial variations in δ, that we tested with CTDAS as well, did not result in applicable transport parameter values, and we discuss them more extensively in the discussion (Chapter 9) instead.

First, we compare a simulation of TM5 as it is currently used (we refer to this as the 'current' TM5 configuration) with a simulation of reduced slopes plus parameterized transport with $\delta = 0.1$ ('new' TM5 configuration). Table 8.1 and Figure 8.1 display the RMSD between model and observations and the actual timeseries at three measurement stations (Alert (ALT), Mauna Loa (MLO), and South Pole (SPO)) for the years 2006 – 2009, respectively.

Table 8.1: RMSD (in ppt) between modeled concentrations and observations for three NOAA (surface) measurement stations. Values with the current TM5 configuration are stated in the left column, values with the new configuration in the right.

	RMSD	
Abbr.	Current TM5	New TM5
ALT	0.108	0.056
MLO	0.049	0.047
SPO	0.046	0.033

It is clear that SF_6 simulations improve on both hemispheres (ALT on NH, SPO on SH) using the new TM5 configuration. In the tropics (MLO), observations were simulated accurately already, and only a minor change is visible. Although these timeseries look promising, we realize that checking three stations is not sufficient to draw conclusion on global SF_6 concentrations. Besides, observations of ALT, MLO, and SPO are used in the assimilation, and it would be better to check our results with independent data.

As a first step, we evaluate timeseries of three independent NOAA aircraft data sets. Table 8.2 provides details on the flights, Table 8.3 displays the RMSD between the modeled and observed concentrations, and Figure 8.2 shows the time series.

For all of them, simulations show a better match with observations using the

Table 8.2: Details on three flights of NOAA aircraft measurement network.

Abbr.	Full name	Country	Latitude	Longitude
DND	Dahlen, North Dakota	United States	47.50	-99.24
PFA	Poker Flat, Alaska	United States	65.07	-147.29
RTA	Rarotonga	Cook Islands	-21.25	-159.83

Table 8.3: RMSD (in ppt) between modeled concentrations and observations for the NOAA aircraft flights from Table 8.2. Values with the current TM5 configuration are stated in the left column, values with the new configuration in the right.

	RMSD	
Abbr.	Current TM5	New TM5
DND	0.092	0.069
PFA	0.057	0.057
RTA	0.051	0.044

new configuration of TM5, and hence suggest that also at high altitudes transport is improved. Yet, the aircrafts flew at specific locations, and conclusions on global concentrations cannot be drawn.

A solution to this is the three-year flight campaign that is known as the HIAPER Pole-to-Pole Observations (HIPPO) project (Wofsy et al., 2012). From 2006 to 2009, an aircraft, equipped to collect data of many different trace gasses (also SF_6), flies from pole to pole and back, along as much longitude bands as possible. On the route, the aircraft deviates its altitude, ranging from 300 up to 14.000 meters. Hereby, Wofsy et al. (2012) present well monitored observations, perfectly suitable to establish a global profile of - in our case - SF_6, which we use to validate our results.

For one of the flights in 2009 we compare observed with modeled SF_6 concentrations (we did not simulate SF_6 for subsequent years, and hence did not consider other flights). Figure 8.3 presents a cross section of the difference between model and observations at different altitudes (up to 11.000m) and a wide range of latitudes (between 70°S and 80°N). Red colors indicate that observed minus modeled values are negative, and that TM5 overestimates measured SF_6 concentrations. Reversely, blue colors indicate an underestimation of the model.

The top figure of the HIPPO data, representing the current configuration of TM5, clearly illustrates the overestimation of observed SF_6 in the NH, and the underestimation in the SH. Reducing the slopes and parameterizing horizontal transport diminish these biases at most altitudes, as the lighter colors in the bottom figure suggest. Moreover, the spatial pattern of over- and underestimation has changes from a sharp gradient into more spread out through the atmosphere.

Overall, we conclude that the new configuration we established for TM5 is suitable to enhance horizontal transport, and hereby improves the global distribution of SF_6. We realize that the match with observations is not perfect yet (slight overestimation in the polar regions, and underestimation in the tropics), and discuss this in the next chapter.

Figure 8.1: Timeseries of SF_6 concentrations, observed and simulated, at three different measurement stations over the years $2006-2009$. From top to bottom: Alert, Nunavut (ALT), Mauna Loa, Hawaii (MLO), and South Pole, Antarctica (SPO). On the left hand side, simulations with the current TM5 configuration are shown. The right hand side displays simulations with the new configuration.

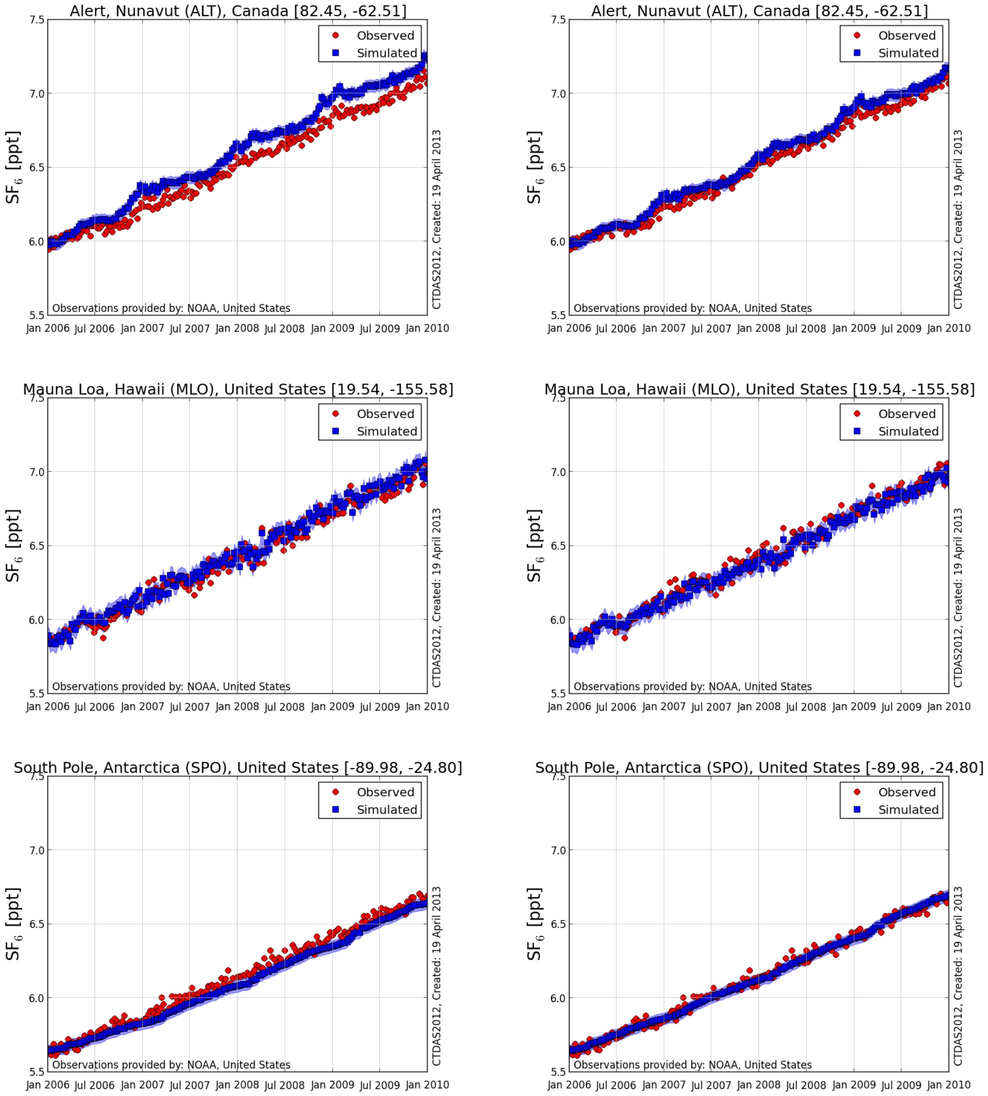

Figure 8.2: Timeseries of SF_6 concentrations, observed and simulated, from free NOAA aircraft flights in the years 2006 – 2009. From top to bottom: Poker Flat, Alaska (PFA), Dahlen, North Dakota (DND), and Rarotonga (RTA). On the left hand side, simulations with the current TM5 configuration are shown. The right hand side displays simulations with the new configuration.

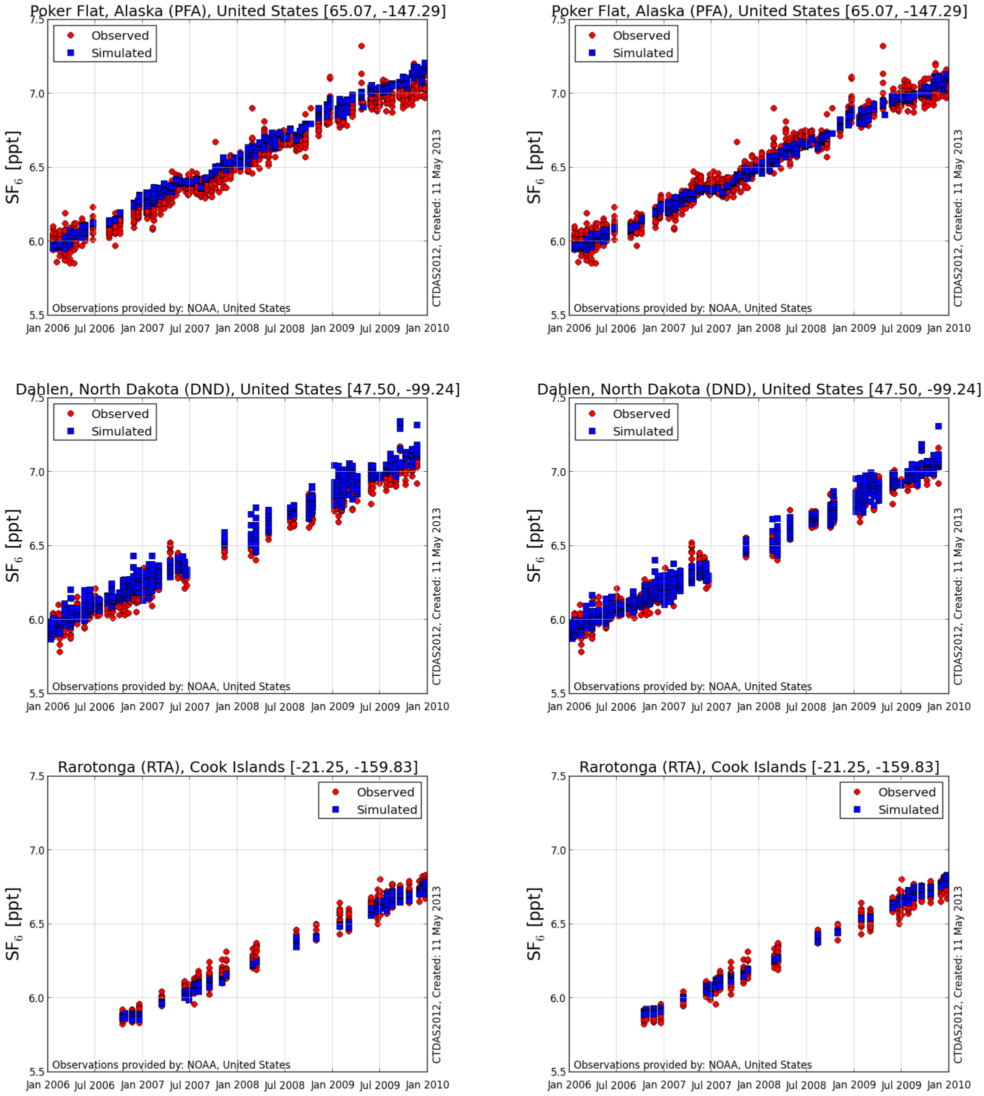

Figure 8.3: Cross sections of SF_6 concentration differences between model and observations at latitudes from 70°S up to 80°N, and altitudes up to 11.000 meters. Concentration differences (observations - modeled values) are given in ppt. The top and bottom figure display SF_6 simulations with the current and new TM5 configuration, respectively.

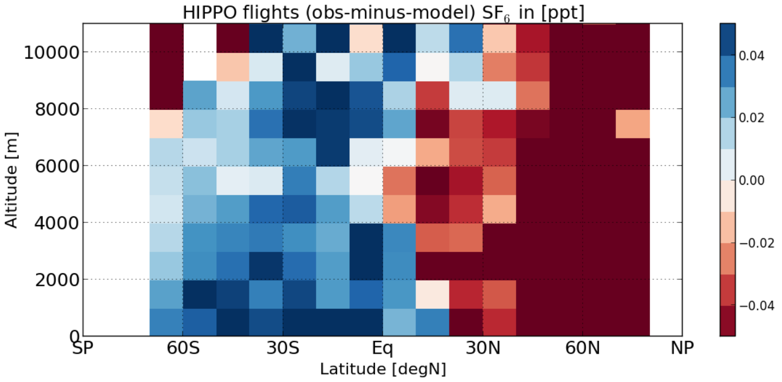

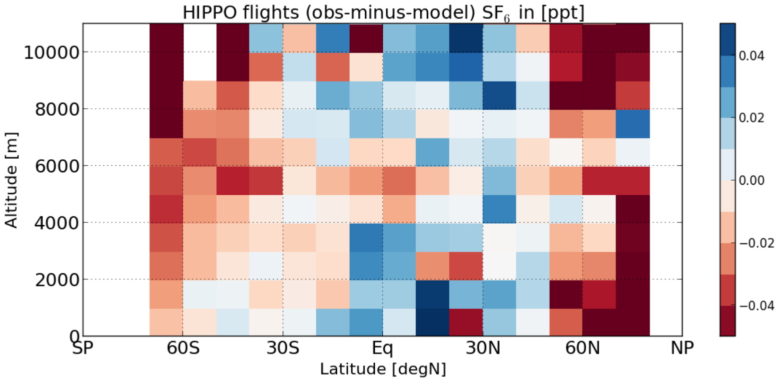

Chapter 9

Discussion

In this chapter we reflect on the research's setup and results. Section 1 evaluates the methods we used to improve interhemispheric transport in TM5. In Section 2 we discuss assumptions for and results from the optimization procedure with the data-assimilation system (CTDAS). Lastly, Section 3 indicates that horizontal diffusion is not sufficient to solve all transport biases in TM5, and that also vertical transport ought to be considered.

1 Consideration on methods

To enhance horizontal transport in TM5 we firstly increased the difusivity of the numerical scheme (in the convection routine). Slopes, determining spatial gradients within a grid box, are updated at each time step. A conservative update results in low difusivity, a less conservative update - that is closer to an upwind scheme - allows more diffusion of tracer. Currently, the slopes in vertical direction are reduced stronger than horizontal ones. We argued that convective updrafts do not distinguish between the direction of the slopes, however, and set the horizontal update equal to the - less conservative - vertical one. We consider equal slope updates as a reasonable argument, and this solves part of the required extra north-south transport of SF_6 as well. Yet, it is not proven that the slopes update that we use for our basecase is the best, and more research is needed to determine the most suitable balance between a conservative slope and a diffuse upwind scheme.

As a second method to enhance interhemispheric mixing, we introduce a parameterization for sub grid scale horizontal diffusion, partly analogous to the work of Prather et al. (1987). According to their work, sub grid horizontal transport occurs near strong convective updrafts, and should be linked to this processes in the model. Herefore, we set a constraint for cloud depth (see equation (6.5)) to trigger the parameterization. This constraint can be considered as a strength, but as a weakness as well. It is good that horizontal transport is enhanced in regions where it occurs in reality. On the other hand, the method works well for tropical and northern mid-latitude regions, but has little impact in southern mid-latitude and polar regions due to the 'lack' of deep convection in these areas. Figure 8.3 shows that enhanced transport improves the global SF_6 distribution. Yet, the overestimation in the polar regions verifies that indeed SF_6 concentrations cannot be transported sufficiently here. Similarly, abundant deep convection in the tropics might cause too strong transport by the parameterization, resulting in the underestimation, represented by the light blue colors. Hence, it might be worth to relax the constraint on cloud depth to allow parameterized transport in polar regions. Furthermore, optimizing transport entirely without the cloud constraint could be useful as well to examine the spatial variation in the diffusion coefficient K (recall that it decreases from the tropics towards the poles and with altitude).

Finally, the diffusion parameterization scheme is resolution dependent. When reducing the grid size, for instance to 3° × 2° (meaning 120 zonal and 90 meridional boxes), we find two opposite effects. On the one hand, a smaller grid size can explicitly solve diffusion, that was sub grid scale before. Extra horizontal transport is less needed, and the parameterization would suffice with a smaller transport parameter. On the other hand, considering equations (6.4), (6.12), and (6.13), reducing the grid box surface area by a factor 4, reduces the diffusion constant, and hence the calculated fluxes as well. A larger transport parameter is needed to account for this.

We briefly tested an optimization of one transport parameter on a 3° × 2° grid. The combination of factors, as explained above, result in a larger δ than found in the same experiment on the larger grid. However, more research is needed to be certain on this, and to find how the dependency applies on other grid sizes.

2 Consideration on optimizing transport

We optimized the transport parameter via data-assimilation with CTDAS. By doing so, we obtained insight in both spatial and temporal variations in horizontal transport linked to convective updrafts, and claim that $\delta = 0.09$ is a suitable transport parameter to implement in TM5 on a 6° × 4° grid. Yet we realize that we had to make certain assumptions in the uptimization procedure, that might have influence the results. We briefly discuss them in this section.

Since we did not want to optimize both fluxes and transport, SF_6 emission fields were fed to the data-assimilation system. The growth rate of SF_6 is rather constant throughout and over the years, and we consider our strategy to match emission fields with the yearly growth rate legitimate. However, we realize that the exact magnitude of emissions, as well as the spatial distribution, is difficult to prescribe exactly. Hence, testing the sensitivity of CTDAS to different emission input files, would be a valuable addition to this research, and could provide better insight in spatial variations in horizontal transport.

Other input data for CTDAS are the weather conditions, provided by ERA-Interim and Operational Data. We verified that the observed concentration gradient of SF_6 between the NH and SH was less overestimated using OD meteorology, than ERA-I. This suggest that, possibly due to higher accuracy in OD, horizontal transport is better represented in OD than in ERA-I. As could be expected, optimized transport parameter values deviated slightly in magnitude between the two data sets. Trends between different CTDAS configurations, however, were comparable. Overall, we state that optimizing transport cannot be done totally independently of meteorological input data. For further TM5 simulations or optimizations with CTDAS, the choice for meteorological input should be considered with care.

Furthermore, optimizations with multiple transport parameters are dependent on the regions in which the parameters are defined. This problem is tightly linked with the cloud depth constraint, as regions without deep convection do not take part in the optimizations procedure. In this research, it was a main reason for the small improvement in simulated concentrations, comparing five to one transport parameter(s). Hence, we state that implementing the five transport parameters, as we found from CTDAS optimizations, gains information on spatial variability of transport, but is not worth the effort of implementation in TM5. However, we believe that there is room for improvement, and that evaluating different regions, in combination with different cloud depth constraints, is a good way to go.

Lastly, we performed our simulations with the gas SF_6. We deem this tracer suitable to test transport in TM5, but strongly suggest to evaluate our procedures and results for other trace gasses (preferably with well known fluxes) as well.

3 Horizontal transport does not solve it all

In this research, solely observations of background stations are used in the assimilation procedure, because they best represent the global distribution of SF_6. Herewith, we determined transport parameters that improve simulated SF_6 concentrations, but cannot eliminate all over- or underestimations. As a test, we assimilate one global transport parameter as before, but now include the - previously independent - NOAA aircraft measurements. In this way, observations at multiple altitudes are represented, which alters the transport parameter's magnitude. Aircraft observations dominate the surface flask network and assimilate transport parameter values up to 0.34 (a factor three higher than without the aircraft data). More mixing is TM5 is required to match observations at high altitudes, but, as we have shown previously, values larger than $\delta = 0.1$ are not suitable to represent surface SF_6. This suggest that stronger transport in TM5 is required, and moreover, that horizontal diffusion cannot solve it all. Hence, we suggest to also investigate the impact of vertical transport in TM5.

Chapter 10

Conclusion

In this research, we evaluate two methods to improve interhemispheric transport of SF_6 in the global chemistry transport model TM5. We show that, by enhancing meridional transport, both overestimations of observed SF_6 concentrations in the Northern Hemisphere, and underestimations of observed SF_6 concentrations in the Southern Hemisphere diminish. Moreover, we find improvements at all latitudes, and in the vertical column (up to 11.000m) as well.

Our first method adjusts the update of horizontal slopes - that determine spatial gradients within a grid box - in the convection routine, to make the numerical scheme more diffuse. This improves TM5's match with observations, but the observed gradient of SF_6 concentrations between the NH and SH is overestimated still. We assume that (unresolved) sub grid transport can solve this problem, and introduce a horizontal diffusion parameterization scheme, largely analogous to the work of Prather et al. (1987). Only in grid boxes where deep convective clouds occur, entrainment and detrainment fluxes (these are turbulent motions, associated with convective updrafts) determine a diffusion coefficient, that is scaled by an arbitrary transport parameter δ to obtain realistic tracer mass fluxes. We aim to find a suitable value for δ, and gain knowledge on temporal and spatial variation in transport as well, by optimizing it with a data-assimilation system (the CarbonTracker Data Assimilation System).

Considering temporal variation, we find that enhancing horizontal transport with the parameterization scheme is most required, and most efficient, in summer months. We explain this process as the 'rectifier effect' (Chan et al., 2008), and identify that it is best captured with seasonally optimized transport (resulting in values of δ slightly smaller, or equal to 0.1). Also, we assess temporal variability by dividing the globe into five regions, and optimize a transport parameter for each of them. The link with convective clouds (as a constraint to trigger the parameterization) prohibits the optimization of transport in the Southern mid-latitudes, and polar regions. Hence, the regions that we determined are not suitable to obtain spatial variation in transport parameters, and more research on the concept is needed.

Overall, we conclude that both the adjusted slopes update and the parameterized diffusion, using one global transport parameter with value $\delta = 0.1$, improve interhemispheric transport in TM5 on a $6° \times 4°$ grid. The parameterization is resolution dependent, and to determine δ for other grid sizes we recommend to iterate our procedures. Lastly, we realize that horizontal transport cannot solve the problem of slow interhemispheric mixing in TM5 alone, and we strongly suggest to explore the impact of vertical diffusion.

Chapter 11

Recommendations

Already in the discussion and conclusion we draw attention to topics that should be researched further. We shortly list them below.

For further research on (improving) interhemispheric mixing in the TM5 transport model, we recommend:

- to (re)consider the slopes update that determines the difusivity of the numerical scheme. We argue that equal updates in all directions should be used, contrary to the current implementation. Which of the updates is most suitable in TM5 should be evaluated in further research.
- further explore the spatial variation in the transport parameter by testing different regions in the optimizations. Possibly, relaxation of the cloud depth constraint may help, since this avoids that certain regions (with little convection) are excluded in the assimilation.
- to test the diffusion parameterization on different grid resolutions. The optimization procedure with CTDAS could be repeated to determine a suitable transport parameter for the desired grid.
- to examine differences between ERA-Interim and Operational Data in (horizontal) transport, and how these might have influenced our transport parameter optimizations.
- to investigate the impact of vertical transport in TM5. We found that TM5's transport bias cannot be solved solely by the enhancement horizontal transport, and we suggest that in addition the role of vertical transport is considered.

Bibliography

Bergamaschi, P., Frankenberg, C., Meirink, J. F., Krol, M., Villani, M. G., Houweling, S., Dentener, F., Dlugokencky, E. J., Miller, J. B., Gatti, L. V., Engel, A., and Levin, I. (2009). Inverse modeling of global and regional CH 4 emissions using SCIAMACHY satellite retrievals. *Journal of Geophysical Research*, 114(D22):D22301.

Berkvens, P. J. F., Botchev, M. A., Lioen, W. M., and Verwer, J. G. (1999). A Zooming Technique for Wind Transport of Air Pollution. Technical report.

Center for Multiscale Modeling of Atmospheric Processes (2013). Entrainment.

Chan, D., Ishizawa, M., Higuchi, K., Maksyutov, S., and Chen, J. (2008). Seasonal CO2 rectifier effect and large-scale extratropical atmospheric transport. *Journal of Geophysical Research*, 113:D17309.

Chatterjee, A. and Michalak, A. M. (2013). Comparison of ensemble Kalman filter and variational approaches for CO2 data assimilation. *Atmospheric Chemistry and Physics Discussions*, 13:12825–12865.

Dee, D. P., Uppala, S. M., Simmons, A. J., Berrisford, P., Poli, P., Kobayashi, S., Andrae, U., Balmaseda, M. A., Balsamo, G., Bauer, P., Bechtold, P., Beljaars, A. C. M., van de Berg, L., Bidlot, J., Bormann, N., Delsol, C., Dragani, R., Fuentes, M., Geer, A. J., Haimberger, L., Healy, S. B., Hersbach, H., Holm, E. V., Isaksen, L., Kallberg, P., Kohler, M., Matricardi, M., McNally, A. P., Monge-Sanz, B. M., Morcrette, J.-J., Park, B.-K., Peubey, C., de Rosnay, P., Tavolato, C., Thepaut, J.-N., and Vitart, F. (2011). The ERA-Interim reanalysis: configuration and performance of the data assimilation system. *Quarterly Journal of the Royal Meteorological Society*, 137:553–597.

Denning, B. A. S., Holzer, M., Gurney, K. R., Heimann, M., Law, R. M., Rayner, P. J., Fung, I. Y., Fan, S.-m., Friedlingstein, P., Balkanski, Y., and Taylor, J. (1999). Three-dimensional transport and concentration of SF A model intercomparison study (TransCom 2). *Tellus*, 51(2):266–297.

EDGAR (2009). Emission Database For Global Atmospheric Research (EDGAR): European Commission, Joint Research Centre (JRC) and Netherlands Environmental Assessment Agency (PBL). *version 4.0*, http://edgar.jrc.ec.europa.eu.

Evensen, G. (1994a). Inverse methods and data assimilation in nonlinear ocean models. *Physica D*, 77(1-3):108–129.

Evensen, G. (1994b). Sequential data assimilation with a nonlinear quasi-geostrophic model using Monte Carlo methods to forecast error statistics. *Journal of Geophysical Research*, 99(C5):10143–10162.

Evensen, G. (2003). The Ensemble Kalman Filter: theoretical formulation and practical implementation. *Ocean Dynamics*, 53(4):343–367.

Gloor, M., Dlugokencky, E., Brenninkmeijer, C., Horowitz, L., Hurst, D. F., Dutton, G., Crevoisier, C., Machida, T., and Tans, P. (2007). Three-dimensional SF 6 data and tropospheric transport simulations: Signals, modeling accuracy, and implications for inverse modeling. *Journal of Geophysical Research*, 112(D15):D15112.

Gurney, K. R., Law, R. M., Denning, a. S., Rayner, P. J., Baker, D., Bousquet, P., Bruhwiler, L., Chen, Y.-H., Ciais, P., Fan, S., Fung, I. Y., Gloor, M., Heimann, M., Higuchi, K., John, J., Maki, T., Maksyutov, S., Masarie, K., Peylin, P., Prather, M., Pak, B. C., Randerson, J., Sarmiento, J., Taguchi, S., Takahashi, T., and Yuen, C.-W. (2002). Towards robust regional estimates of CO2 sources and sinks using atmospheric transport models. *Nature*, 415(6872):626–30.

Houtekamer, P. L. and Mitchell, H. L. (1998). Data Assimilation Using an Ensemble Kalman Filter Technique. *Monthly Weather Review*, 126(3):796–811.

Krol, M., Houweling, S., Bregman, B., van den Broek, M., Segers, a., van Velthoven, P., Peters, W., Dentener, F., and Bergamaschi, P. (2005). The two-way nested global chemistry-transport zoom model TM5: algorithm and applications. *Atmospheric Chemistry and Physics*, 5(2):417–432.

Morton, K. W. and Mayers, D. F. (2005). *Numerical Solution of Partial Differential Equations*. Cambridge University Press, Cambridge, second edition.

Peters, W., Krol, M., Dlugokencky, E. J., Dentener, F. J., Bergamaschi, P., Dutton, G., van Velthoven, P., Miller, J. B., Bruhwiler, L., and Tans, P. P. (2004). Toward regional-scale modeling using the two-way nested global model TM5: Characterization of transport using SF 6. *Journal of Geophysical Research*, 109(D19):D19314.

Peters, W., Miller, J. B., Whitaker, J., Denning, a. S., Hirsch, a., Krol, M. C., Zupanski, D., Bruhwiler, L., and Tans, P. P. (2005). An ensemble data assimilation system to estimate CO 2 surface fluxes from atmospheric trace gas observations. *Journal of Geophysical Research*, 110(D24).

Pisso, I., Real, E., Law, K. S., Legras, B., Bousserez, N., Attié, J. L., and Schlager, H. (2009). Estimation of mixing in the troposphere from Lagrangian trace gas reconstructions during long-range pollution plume transport. *Journal of Geophysical Research*, 114(D19):D19301.

Prather, M., Mcelroy, M., Wofsy, S., Russell, G., and Rind, D. (1987). Chemistry of the Global Troposphere: Fluorocarbons as Tracers of Air Motion. *Journal of Geophysical Research*, 92(D6):6579–6613.

Ravishankara, A. R., Solomon, S., Turnipseed, A. A., and Warren, R. F. (1993). Atmospheric lifetimes of long-lived halogenated species. *Science (New York, N.Y.)*, 259(5092):194–199.

Russell, G. L. and Lerner, J. A. (1981). A New Finite-Differencing Scheme for the Tracer Transport Equation. *Journal of Applied Meteorology*, 20:1483–1498.

Stephens, B. B., Gurney, K. R., Tans, P. P., Sweeney, C., Peters, W., Bruhwiler, L., Ciais, P., Ramonet, M., Bousquet, P., Nakazawa, T., Aoki, S., Machida, T., Inoue, G., Vinnichenko, N., Lloyd, J., Jordan, A., Heimann, M., Shibistova, O., Langenfelds, R. L., Steele, L. P., Francey, R. J., and Denning, a. S. (2007). Weak northern and strong tropical land carbon uptake from vertical profiles of atmospheric CO2. *Science (New York, N.Y.)*, 316(5832):1732–5.

Verwer, J. G., Spee, E. J., Blom, J. G., and Hundsdorfer, W. (1999). A second-order Rosenbrock method applied to photochemical dispersion problems.pdf. *SIAM J. Sci. Comp.*, 20(4):1456–1480.

Wofsy, S. C., Daube, B. C., Jimenez, R., Kort, E., Pittman, J. V., Park, S., Commane, R., Xiang, B., Santoni, G., Jacob, D., Fisher, J., Pickett-Heaps, C., Wang, H., Wecht, K., Wang, Q.-Q., Stephens, B. B., Shertz, S., Watt, A. S., Romashkin, P., Campos, T., Haggerty, J., Cooper, W. A., Rogers, D., Beaton, S., Hendershot, R., Elkins, J. W., Fahey, D. W., Gao, R. S., Moore, F., Montzka, S. A., Schwarz, J. P., Perring, A. E., Hurst, D., Miller, B. R., Sweeney, C., Oltmans, S., Nance, D., Hintsa, E., Dutton, G., Watts, L. A., Spackman, J. R., Rosenlof, K. H., Ray, E. A., Hall, B., Zondlo, M. A., Diao, M., Keeling, R., Bent, J., Atlas, E. L., Lueb, R., and Mahoney, M. J. (2012). HIPPO Combined Discrete Flask and GC Sample GHG, Halo-, Hydrocarbon Data (R_20121129). *Carbon Dioxide Information Analysis Center, Oak Ridge National Laboratory, Oak Ridge, Tennessee, U.S.A.*

Yin, X. (2000). Surface Wind Speed over Land: A Global View. *Journal of Applied Meteorology*, 39:1861–1865.

Zipser, E. J. (1969). The role of organized unsaturated convective downdrafts in the structure and rapid decay of an equatorial disturbance.pdf. *Journal of Applied Meteorology*, 8:799–813.

Appendix A

Derivation of an appropriate run time

In Chapter 3 we set up a simple transport model, that is used later on in a data-assimilation test experiment. Besides the default settings, as determined in Section 2, an appropriate run time and time step are required. They need to be such such that the exponential decay of the concentration is captured, without reaching the steady state too early in the experiment. Herefore, we performed a dimensional analysis of the advection-diffusion equation. The resulting derivation for t_{end}, assuming $t_0 = 0.0$, is explained below.

We start off with a commonly used method for partial differential equations: separation of variables. The concentration is written as the product of a function of space and a function of time:

$$c(x,t) = X(x) \cdot T(t). \tag{A.1}$$

Here, $c(x,t)$ is the concentration for a point in space x, and in time t.

Substituting this into equation (3.1) provides:

$$\frac{T'}{T} = D\frac{X''}{X} - u\frac{X'}{X}, \tag{A.2}$$

with T' the first derivative of T with respect to t, X' and X'' the first and second derivatives of X with respect to x, respectively.

Since the left hand side of (A.2) depends on t, and the right hand side on x, they are independent terms. For them to be equal, they must be a constant value, say $-\lambda$. From this, we obtain two ordinary differential equations:

$$T' + \lambda T = 0, \tag{A.3}$$

for the left hand side, and:

$$DX'' - uX' + \lambda X = 0, \tag{A.4}$$

for the right hand side. Recall that u is the advection, and D the diffusion coefficient.

Now, we derive the boundary conditions by substituting (A.1) in (3.4) and (3.5):

$$\begin{array}{rrcll} & c(0,t) & = & c(L,t) & \forall t; \\ \Leftrightarrow & X(0)\cdot T(t) & = & X(L)\cdot T(t) & \forall t; \\ \Leftrightarrow & X(0) & = & X(L), & \end{array} \tag{A.5}$$

and:

$$\begin{array}{lrcll} & c_x(0,t) & = & c_x(L,t) & \forall t; \\ \Leftrightarrow & X'(0)\cdot T(t) & = & X'(L)\cdot T(t) & \forall t; \\ \Leftrightarrow & X'(0) & = & X'(L). & \end{array} \tag{A.6}$$

With these boundary conditions, we can solve the differential equation for X. The general form would be:

$$X(x) = d_1 e^{r_1 x} + d_2 e^{r_2 x}, \tag{A.7}$$

with d_1 and d_2 arbitrary constants. The according characteristic equation for the differential equation is:

$$Dr^2 - ur + \lambda = 0, \tag{A.8}$$

such that:

$$r_1, r_2 = \frac{u \pm \sqrt{u^2 - 4D\lambda}}{2D}. \tag{A.9}$$

For the default settings of our simple transport model, this becomes:

$$r_1, r_2 = \frac{3 \pm \sqrt{9 - 4\lambda_n}}{2}, \tag{A.10}$$

Evaluating (A.7) for the boundary conditions, provides the following constraints:

$$\begin{array}{lrclcrcl} & e^{r_1 x} & = & 1 & \text{or} & e^{r_2 x} & = & 1; \\ \Leftrightarrow & r_1 L & = & 0 + 2in\pi & \text{or} & r_1 L & = & 0 + 2in\pi; \\ \Leftrightarrow & \frac{u+\sqrt{u^2-4D\lambda_n}}{2D} & = & \frac{2ni\pi}{L} & \text{or} & \frac{u-\sqrt{u^2-4D\lambda_n}}{2D} & = & \frac{2ni\pi}{L}. \end{array} \tag{A.11}$$

From this, we determine the eigenvalues λ_n ($\forall n \in \mathbb{N}$) for a general case, followed by the eigenvalues for the default settings of Section 2:

$$\begin{array}{rcl} \lambda_n & = & \frac{u^2-(4inpiD/L-u)^2}{4D}, \\ & = & \frac{4n^2\pi^2 D}{L^2} + \frac{2in\pi}{L}, \\ & = & 4n^2\pi^2 + 6in\pi, \end{array} \tag{A.12}$$

Since $\lambda_n > 2.5$ for $n > 1$, we find from (A.10) that r_1 are r_2 are imaginary numbers. Hence, we may write:

$$\begin{array}{rl} X_n(x) & = d_1 e^{(\alpha+i\beta)x} + d_2 e^{(\alpha-i\beta)x}, \\ & = e^{\alpha}\left(d_1 e^{i\beta x} + d_2 e^{-i\beta x}\right), \\ & = d_3 \cdot \cos(\beta x), \end{array} \tag{A.13}$$

with d_3 an arbitrary constant, $\alpha = \frac{3}{2}$, and $\beta = \frac{1}{2}\sqrt{9 - 4\lambda_n}$.

Next step is to solve the differential equation for T. It has the general form:

$$\begin{array}{rl} T_n(t) & = d_4 e^{-\lambda_n t}, \\ & = d_4 e^{-(4n^2\pi^2+6in\pi)t}, \\ & = d_4\left(\cos(6n\pi t) - i\sin(6n\pi t)\right) e^{-4n^2\pi^2 t}, \end{array} \tag{A.14}$$

with again d_4 an arbitrary constant. From the solutions for X and T we obtain the overall solution for the concentration as follows:

$$c(x,t) = \sum_{n=1}^{\infty} \tilde{d_n} \cos\left(\frac{\sqrt{9-4\lambda_n}}{2} \cdot x\right)\left(\cos(6n\pi t) - i\sin(6n\pi t)\right) e^{-4n^2\pi^2 t}, \tag{A.15}$$

with $\tilde{d_n}$ constants determined by d_3, d_4, and the initial condition. From (A.15) we see that the concentration is in two ways dependent on time. The first are oscillations, caused by the sine and cosine function. Besides, we have an exponential decay of concentration, caused by the negative exponential. The last is of main interest, when considering the run time for the experiment. Namely, we would like to see clearly the decay of concentrations, without arriving at the steady state far before the end time. The smallest (real part of the) eigenvalue, $4n^2\pi^2$, determines the slowest decay. For instance, e^{-2t} decreases faster than e^{-t}. For our case we find that the decay of concentrations is slowest for $n = 1$, such that we have: $e^{-4\pi^2 t}$. The characteristic time scale, which is one divided by the smallest (real part of the) eigenvalue, should be of the same order as the end time in order to accomplish our requirements. We find $\frac{1}{4\pi^2} \approx 0.025$, but realize that in our experiment different values for D are used. This will shorten or extend the characteristic time scale for those experiments. To be sure to capture the whole decay, we take a large value for t_{end} that still remains within the order of the characteristic time scale: $t_{end} = 0.1$.

Lastly, we provide a short remark on the oscillations. In order not to miss them in the concentration profile, it is important that the time step is much smaller than the length of one period divided by the argument of the sine and cosine:

$$\Delta t \ll \frac{2\pi}{6\pi} = \frac{1}{3}. \tag{A.16}$$

Verifying with Section 2 shows that $\Delta t = 1.0e\text{-}4$ is indeed a suitable time step to capture the oscillations.

It is important to realize that the above time step is calculated for $n = 1$. For higher n, one would expect a smaller time step. However, the negative exponential would then dominate the effect of oscillations, such that the time step length is just important for the stability of the numerical scheme, but not so much for the effect of oscillations.

Appendix B

NOAA surface flask network

Here, we provide an overview of the NOAA surface flask network's stations for SF_6. Abbreviations and full names are listed below. On the next page we show the locations of the stations in a global map. Note that the red stations are considered as background stations (indicated with B below), and hence included in the optimizations. The blue dots are not, since they are influenced by local SF_6 sources.

Table B.1: Overview of measurement stations (Part 1).

Abbr.	Full name	Country	Latitude	Longitude
ABP	Arembepe, Bahia	Brazil	-12.77	-38.17
ALT (B)	Alert, Nunavut	Canada	82.45	-62.51
ASC (B)	Ascension Island	United Kingdom	-7.97	-14.40
ASK (B)	Assekrem	Algeria	23.18	5.42
AZR (B)	Terceira Island, Azores	Portugal	38.77	-27.38
BAL	Baltic Sea	Poland	55.35	17.22
BHD (B)	Baring Head Station	New Zealand	-41,41	174,87
BKT (B)	Kototabang	Indonesia	-0.20	100.32
BME	St. Davids Head, Bermuda	United Kingdom	32.37	-64.65
BMW (B)	Tudor Hill, Bermuda	United Kingdom	32.26	-64.88
BRW (B)	Barrow, Alaska	United States	71.32	-156.61
BSC	Black Sea, Constanta	Romania	44.18	28.66
CBA (B)	Cold Bay, Alaska	United States	55.21	-162.72
CGO (B)	Cape Grim, Tasmania	Australia	-40.68	144.69
CHR (B)	Christmas Island	Republic of Kiribati	1.70	-157.15
CPT	Cape Point	South Africa	-34.35	18.49
CRZ (B)	Crozet Island	France	-46.43	51.85
EIC (B)	Easter Island	Chile	-27.16	-109.43
GMI (B)	Mariana Islands	Guam	13.39	144.66
HBA (B)	Halley Station, Antarctica	United Kingdom	-75.61	-26.21
HPB	Hohenpeissenberg	Germany	47.80	11.02
HUN	Hegyhatsal	Hungary	46.95	16.65
ICE (B)	Storhofdi, Vestmannaeyjar	Iceland	63.40	-20.29
IZO (B)	Tenerife, Canary Islands	Spain	28.31	-16.50

Table B.2: Overview of measurement stations (Part 2).

Abbr.	Full name	Country	Latitude	Longitude
KEY	Key Biscayne, Florida	United States	25.67	-80.16
KUM (B)	Cape Kumukahi, Hawaii	United States	19.52	-154.82
KZD	Sary Taukum	Kazakhstan	44.08	76.87
KZM	Plateau Assy	Kazakhstan	43.25	77.88
LLB	Lac La Biche, Alberta	Canada	54.95	-112.45
LMP	Lampedusa	Italy	35.52	12.62
MEX	High Altitude Global Climate Observation Center	Mexico	18.98	-97.31
MHD	Mace Head, County Galway	Ireland	53.33	-9.90
MID	Sand Island, Midway	United States	28.21	-177.38
MKN	Mt. Kenya	Kenya	-0.06	37.30
MLO (B)	Mauna Loa, Hawaii	United States	19.54	-155.58
NMB (B)	Gobabeb	Namibia	-23.58	15.03
NWR	Niwot Ridge, Colorado	United States	40.05	-105.59
OXK	Ochsenkopf	Germany	50.03	11.81
PAL	Pallas-Sammaltunturi, GAW Station	Finland	67.97	24.12
POC (B)	Pacific Oceann	-	-	-
PSA (B)	Palmer Station, Antarctica	United States	-64.92	-64.00
PTA	Point Arena, California	United States	38.95	-123.74
RPB (B)	Ragged Point	Barbados	13.16	-59.43
SEY (B)	Mahe Island	Seychelles	-4.68	55.53
SGP	Southern Great Plains, Oklahoma	United States	36.61	-97.49
SHM (B)	Shemya Islands, Alaska	United States	52.71	174.13
SMO (B)	Tutuila	American Samoa	-14.25	-170.56
SPO (B)	South Pole, Antarctica	United States	-89.98	-24.80
STM	Ocean Station M	Norway	66.00	2.00
SUM (B)	Summit	Greenland	72.60	-38.42
SYO (B)	Syowa Station, Antarctica	Japan	-69.00	39.58
TAP	Tae-ahn Peninsula	Republic of Korea	36.74	126.13
TDF	Tierra Del Fuego, Ushuaia	Argentina	-54.85	-68.31
THD	Trinidad Head, California	United States	41.05	-124.15
UTA	Wendover, Uta	United States	39.90	-113.72
UUM	Ulaan Uul	Mongolia	44.45	111.10
WIS	WIS Stations, Negev Desert	Israel	30.86	34.78
WLG	Mt. Waliguan	Peoples Rep. China	36.29	100.90
ZEP (B)	Ny-Alesund, Svalbard	Norway and Sweden	78.91	11.89

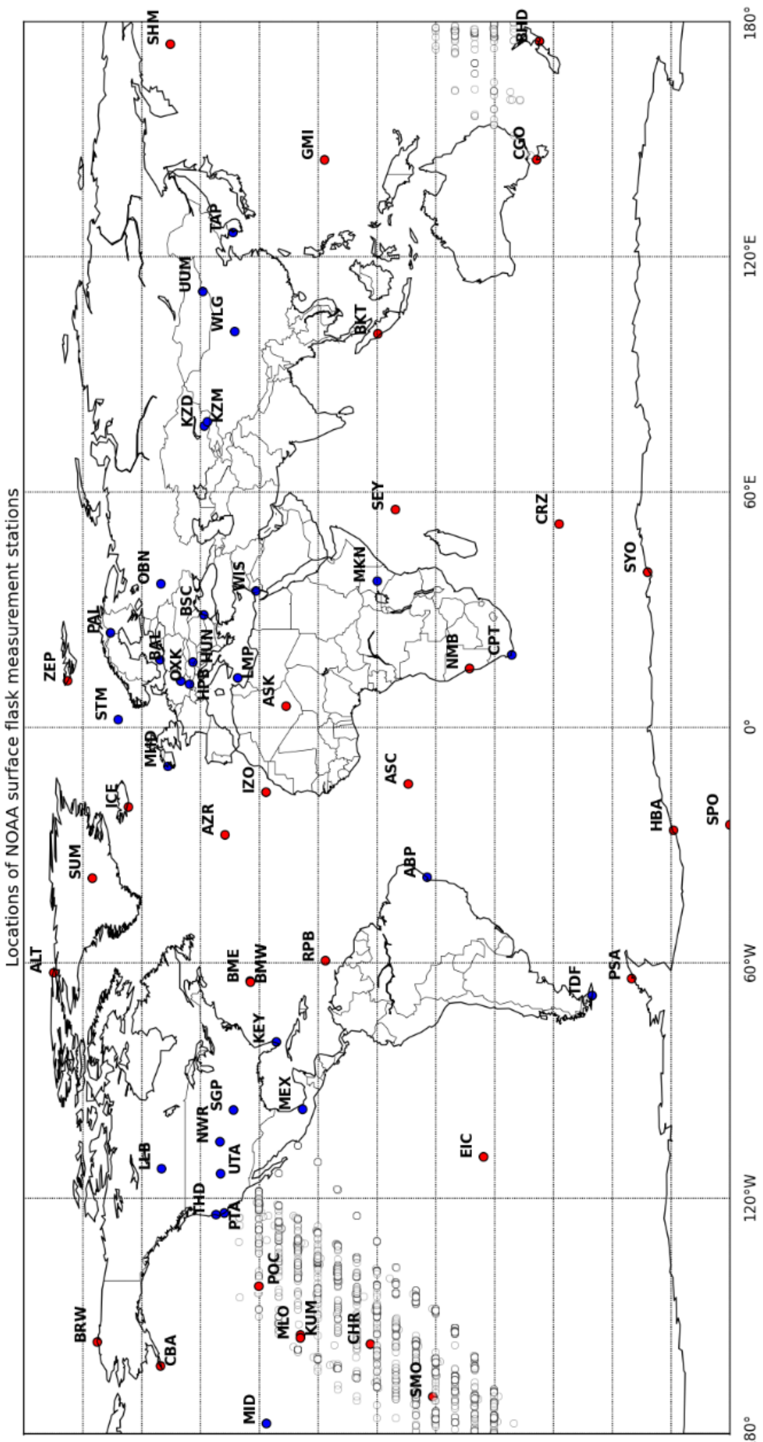

Figure B.1: NOAA surface flask network for SF_6. Red dots represent background stations (indicated with (B) in Table B.1 and B.2), of which observations are included in the optimization. Observations of others, shown as blue dots, are not. Note that 'POC' is a ship, and its measurements are collected throughout the Pacific Ocean.

Appendix C

RMSD after optimization

Figure C.1: RMSD of forward runs with one transport parameter: $\delta = 0.15$ (blue), $\delta = 0.1$ (yellow), and $\delta = 0.08$ (red).

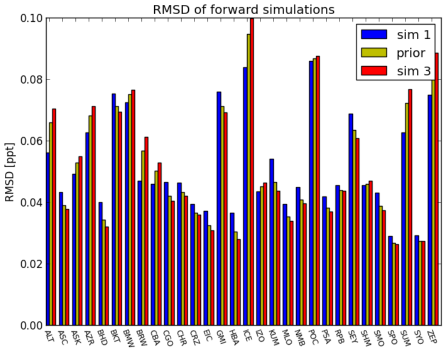

Figure C.2: RMSD of forward runs with five transport parameters: $\delta = [0.15, 0.37, 0.10, 0.13, 0.13]$ (blue), $\delta = [0.1, 0.1, 0.1, 0.1, 0.1]$ (yellow), and $\delta = [0.10, 0.18, 0.07, 0.10, 0.10]$ (red).

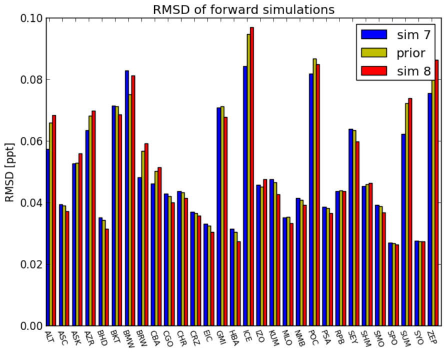

Appendix D

Cloud meteorology in ERA-Interim

Figure D.1: Convective precipitation in $10^{-7}\frac{m}{s}$ on a 1° × 1° grid in January (left) and July (right) 2008. Maps are obtained from ERA-Interim meteorological data and representative for the same months in other years.

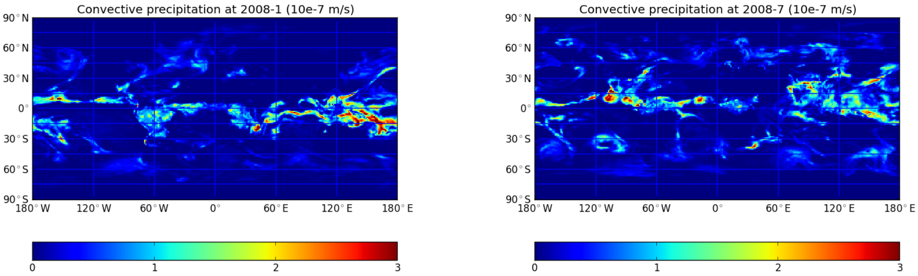

Figure D.2: Cloud depth in hPa as calculated in TM5 on a 6° × 4° grid in January (left) and July (right) 2008, but representative for other years as well.